Remote Sensing of Environment 341 (2026) 115443

Contents lists available at ScienceDirect

Remote Sensing of Environment

journal homepage: www.elsevier.com/locate/rse

Improved vegetation optical depth retrievals based on LAI climatology and dynamic surface roughness

Hui Zhang [a,b], Zhou Shi [a,b], Lun Gao [c], Zhibin Sun [d], Bing He [e], Yixiang Wang [f,g,h], Hongquan Wang [i,*]

[a] State Key Laboratory of Soil Pollution Control and Safety, Zhejiang University, Hangzhou 310058, China
[b] Zhejiang Key Laboratory of Agricultural Remote Sensing and Information Technology, College of Environmental and Resource Sciences, Zhejiang University, Hangzhou 310058, China
[c] Institute on the Environment, University of Minnesota, St. Paul, MN 55108, USA
[d] School of Mathematical Sciences, Ministry of Education Key Laboratory of NSLSCS, Nanjing Normal University, Nanjing, 210023, China
[e] School of Computer Science, Chengdu University of Information Technology, Chengdu 610225, China
[f] State Key Laboratory of Subtropical Silviculture, Zhejiang A&F University, Hangzhou 311300, China
[g] Key Laboratory of Carbon Cycling in Forest Ecosystems and Carbon Sequestration of Zhejiang Province, Zhejiang A&F University, Hangzhou 311300, China
[h] College of Environment and Resource Sciences, Zhejiang A&F University, Lin'an 311300, Zhejiang, China
[i] Agriculture and Agri-Food Canada Lethbridge Research and Development Centre, Lethbridge, AB, Canada

ARTICLE INFO

Edited by: Jing M. Chen

Keywords:
τ-ω model
Vegetation optical depth
Passive microwave
SMAPVEX16
SMAPVEX12

ABSTRACT

L-band vegetation optical depth (VOD) from NASA's Soil Moisture Active Passive (SMAP) mission is widely used to study carbon, water, and energy exchange. Its retrieval relies on the τ-ω radiative transfer model, constrained by Normalized Difference Vegetation Index (NDVI) climatology and a constant surface roughness parameter (H_{rp}). However, constant H_{rp} fails to capture dynamics from agricultural practices and weather, while NDVI saturates under dense canopies and cannot directly reflect vegetation structure. To address these limitations, we propose a new algorithm that incorporates leaf area index (LAI) climatology and its dynamic H_{rp} into the constrained multi-channel algorithm (CMCA) that can account for smooth temporal vegetation variations, with the final aim to improve VOD retrievals by optimizing H_{rp} parameterization and prior information of VOD. Based on Passive Active L-band Sensor (PALS) data from SMAPVEX16-MB, we first evaluated four H_{rp} parametrization schemes across three well-developed algorithms (the regularized dual-channel algorithm (RDCA), the multi-temporal dual-channel algorithm (MT-DCA), and CMCA). The schemes include two constant models based on surface geometry, one dynamic model based on LAI and brightness temperature (TB), and the original algorithm parameterization. Then, we assessed measured LAI and NDVI climatology as prior information for constraining VOD, demonstrating that measured LAI provides more accurate VOD estimates due to its superior characterization of vegetation water content (VWC) and biomass dynamics. Synergistically upscaling field-based LAI and H_{rp} to satellite footprint-scale consistently enhanced the three algorithms, though to varying degrees, with retrieved dynamic H_{rp} via VOD determined by LAI climatology. We found that the CMCA performs best, with the correlation coefficients (R) between VOD and VWC/biomass across the three crops ranging from 0.73 to 0.88 and 0.84–0.88, respectively. This improvement stems from the better ability of LAI climatology to capture VWC and biomass variations than NDVI climatology, the physical constraints in CMCA, and the dynamic H_{rp} that characterizes surface roughness. The proposed algorithms were validated against vegetation water content and biomass measurements from SMAPVEX12. Results suggest that LAI climatology can significantly improve VOD retrieval from SMAP observations: R values between VOD and VWC/biomass were 0.71–0.81/0.68–0.90 for the improved algorithm versus 0.38–0.81/0.37–0.94 for the original. Overall, this study highlights the importance of incorporation LAI and dynamic roughness parameter for improved VOD retrieval, which is essential for carbon cycle studies dependent on accurate vegetation dynamics.

* Corresponding author at: Agriculture and Agri-Food Canada Lethbridge Research and Development Centre, 5403 1 Ave S, Lethbridge, AB, Canada.
E-mail address: hongquan.wang@agr.gc.ca (H. Wang).

https://doi.org/10.1016/j.rse.2026.115443
Received 25 March 2025; Received in revised form 17 February 2026; Accepted 20 April 2026

1. Introduction

A better understanding of the exchanges of carbon, water, and energy between land surfaces and the atmosphere is crucial for global climate and ecosystem research (Pan et al., 2014; Hamilton and Friess, 2018; Abbott et al., 2019). As a key parameter in the zero-order solution of the microwave radiative transfer (RT) equation (i.e., the τ-ω model), vegetation optical depth (VOD) quantifies how vegetation layers attenuate microwave radiation emitted or reflected by Earth's surface (Mo et al., 1982; Pardé et al., 2003; Wigneron et al., 2017). Estimated by passive microwave measurements, VOD is closely related to vegetation water content (VWC) and aboveground biomass, making it a promising tool for such studies (Scholze et al., 2019; Kumar et al., 2020; Wigneron et al., 2020; Wang et al., 2021a). Numerous large-scale studies of land-atmosphere exchanges and ecosystem sustainability have been supported by VOD (Brandt et al., 2018; Fan et al., 2019; Kumar et al., 2020; Fan et al., 2024; Poulter et al., 2025). For example, VOD has been used to simulate ecosystem functional properties (e.g., gross primary productivity, light use efficiency, evapotranspiration, and biospheric carbon dioxide exchange) (Kumar et al., 2020; Laurin et al., 2020; Poulter et al., 2025), monitor biomass (Liu et al., 2015; Brandt et al., 2018; Rodríguez-Fernández et al., 2018; Fan et al., 2019; Fan et al., 2024), analyze phenology (Jones et al., 2014; Dannenberg et al., 2020), and track drought and vegetation conditions (Momen et al., 2017; Laurin et al., 2020; Zotta et al., 2023).

L-band microwave offers better penetration than higher microwave frequencies (K-band, X-band, or C-band), making it more effective for monitoring vegetation with moderate to dense cover. NASA's Soil Moisture Active Passive (SMAP) and ESA's Soil Moisture and Ocean Salinity (SMOS) satellite missions (Kerr et al., 2010; Entekhabi et al., 2010) utilize L-band sensors to detect VOD and soil moisture (SM). These missions typically use the τ-ω model to account for the interactions between soil emission and vegetation canopy layer. The τ-ω model describes top-of-atmosphere emission as a summation of three components: i) upwelling soil emission propagated through the vegetation; ii) upwelling emission from the vegetation; and iii) downward emission from vegetation reflected by soil and attenuated by the vegetation.

In this model, soil emission is related to rough surface reflectivity, which is modeled in relation to smooth surface reflectivity and surface roughness parameters using the semi-empirical HQN roughness model, with a critical roughness parameter H_{rp} (Wang and Choudhury, 1981; Wigneron et al., 2001; Escorihuela et al., 2007; Wigneron et al., 2017). Smooth surface reflectivity is derived from the Fresnel equations, which require soil dielectric constant and observation angle (Mironov et al., 2009; Mironov et al., 2017; Wang et al., 2021b). The Mironov dielectric model uses soil temperature and clay fraction to convert soil dielectric constant to SM (Mironov et al., 2009; Mironov et al., 2017). In SMAP algorithms, soil texture and temperature source from the 250 m SoilGrid dataset and the Goddard Modeling and Assimilation Office (GMAO) model, respectively (O'Neill et al., 2020). Furthermore, SMAP retrieval algorithms assume isothermal conditions for surface and vegetation temperatures during the overpass at local 6:00 AM (O'Neill et al., 2015), both of which are parameterized using the effective soil temperature, i.e., a weighted average of the top two soil layers. This approach follows the methodology of Choudhury et al. (1982), using soil temperature forecasts from the NASA Goddard Space Flight Center GEOS-5 model.

In contrast, VOD and single scattering albedo are used to parameterize vegetation-induced extinction (absorption and scattering) and scattering above the soil, respectively, both of which are associated with VWC and canopy architecture (Ulaby and Jedlicka, 1984; Jackson and Schmugge, 1991; Chahuan et al., 1994; Kurum, 2013; Long and Ulaby, 2015; Gao et al., 2020a). VOD derived from low-frequency bands (L-band, C-band, and X-band) shows insensitivity to atmospheric influences, clouds, and solar radiation (Li et al., 2021), and its retrieval algorithms vary by band: for L-band VOD, which is primarily derived from the aforementioned SMOS and SMAP observations, SMOS uses official Level 2 (L2) and Level 3 (L3) algorithms (Kerr et al., 2012; Al Bitar et al., 2017), while SMAP uses the dual-channel algorithm (DCA) and its regularized modification, the regularized dual-channel algorithm (RDCA)—both proposed and improved successively (O'Neill et al., 2020; Chaubell et al., 2021). By comparison, C-band and X-band VOD are primarily derived from the Advanced Microwave Scanning Radiometer for EOS (AMSR-E) (2002−2012) and Advanced Microwave Scanning Radiometer 2 (AMSR2) (2012-present), retrieved mainly via the land parameter data record (LPDR) algorithm (Du et al., 2017) and the land parameter retrieval model (LPRM) algorithm (Owe et al., 2001; Owe et al., 2008).

Due to the single observation angle and frequency channel in SMAP, retrieving target parameters (VOD and SM) faces ill-conditioning, as dual-polarization brightness temperatures (TBs) show strong correlation (Montpetit et al., 2015; Konings et al., 2016; Gao et al., 2020a, 2020b, 2020c; Wang et al., 2021a). To address this, a priori knowledge of single scattering albedo and H_{rp} is often incorporated as known inputs, typically pre-determined as constants based on land covers, with values calibrated through early numerical experiments or field campaigns (Chaubell et al., 2020; O'Neill et al., 2020). Alternatively, they can be directly inverted from the τ-ω model using multiple spatiotemporal observations or by fixing SM/VOD (Konings et al., 2016; Vittucci et al., 2017; Chaubell et al., 2020; Gao et al., 2020b). Additionally, H_{rp} can be decoupled from TR—a single parameter combining vegetation and roughness effects—based on the TR-LAI linear relationship, with TR and SM retrieved simultaneously via τ-ω inversion (Parrens et al., 2016). When compared with the surface roughness parameter, the weak scattering effects within vegetation contribute less to TB (Wigneron et al., 2004; Kurum, 2013; Karthikeyan et al., 2019). As a result, TB is primarily influenced by the combined effects of VOD and H_{rp}, along with SM.

Diverse algorithms have been developed for the SMAP mission with two strategies often employed to handle VOD (Gao et al., 2021): (1) direct calculation using VWC derived from NDVI climatology and land cover-specific b values in single-channel algorithms (SCA) (Jackson, 1993; Bindlish et al., 2015), and (2) simultaneous retrieval together with SM in dual-channel algorithms (DCA) (Njoku et al., 2003). With advancements in retrieval algorithms, strategies have evolved to incorporate physical constraints and assumptions as a priori information, helping mitigate spatiotemporal noise and resolve ill-posed problems (Gao et al., 2021). Specifically, the regularized DCA (RDCA) improves stability by introducing a regularization term for VOD based on NDVI climatology, mitigating the impact of spatiotemporal noise (O'Neill et al., 2020). Multi-temporal DCA (MT-DCA) assumes constant VOD over a week and uses multi-temporal observations to enhance accuracy (Konings et al., 2017). To tackle the ill-posed problem caused by highly correlated polarized emissivity and consider the smooth temporal changes in VOD, the constrained multi-channel algorithm (CMCA) integrates Tikhonov (Tikhonov, 1963) and Sobolev-norm regularizations (Adams and Fournier, 2003) into MT-DCA, imposing box constraints to ensure that the retrieval aligns with the phenology of VWC (using NDVI climatology) and SM retention capacity (Ebtehaj and Bras, 2019; Gao et al., 2020c). In this study, VOD retrieval was attempted using an approach similar to Baur et al. (2019) and Wang et al. (2021a). This approach retrieves only a vegetation parameter, while SM is derived from ancillary data. The single-parameter retrieval avoids the redundancy-induced issue mentioned above; however, it still suffers from retrieval errors due to observational or modeling noise. It is worth noting that NDVI climatology is used to constrain VOD in both SMAP official algorithms (e.g., SCA and RDCA) and other mainstream algorithms (e.g., CMCA).

Therefore, a priori information on VOD is of crucial importance, although its performance varies with inversion strategies. However, NDVI tends to be saturated easily and its climatology fails to capture changes resulting from agricultural practices or extreme events such as

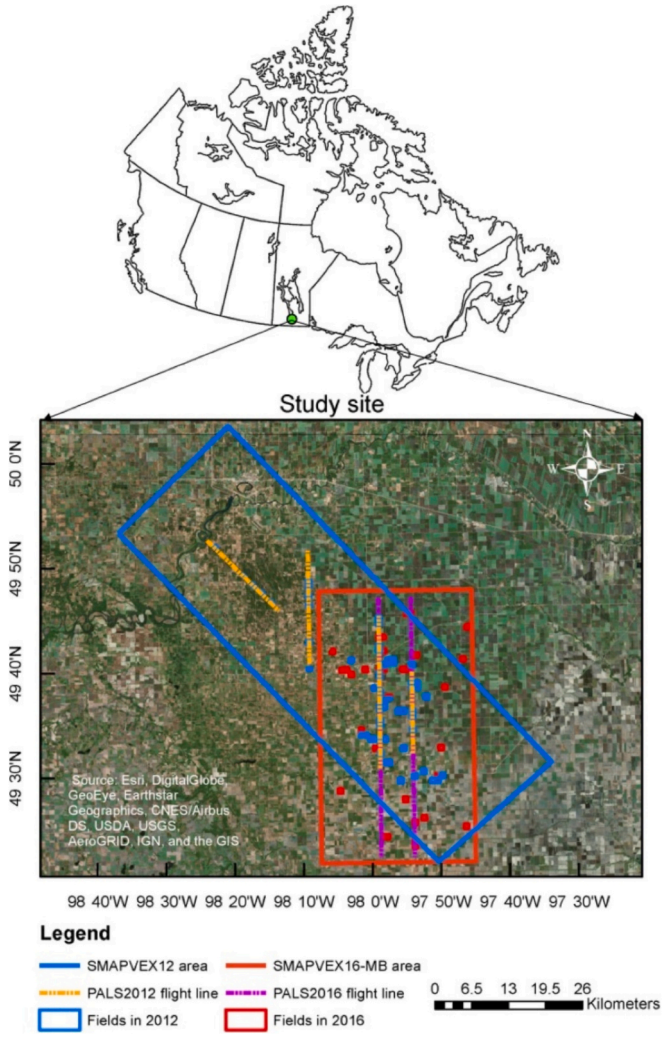

Fig. 1. PALS flight lines and in-situ measured agricultural fields during the SMAPVEX16-MB campaigns and SMAPVEX12 in Manitoba, Canada (Wang et al., 2021b).

forest fires, which can introduce significant uncertainties in SMAP retrievals (Jiang et al., 2008; Konings et al., 2017; Zeng et al., 2022; Feng et al., 2025).

Previous studies have shown that VOD is closely associated with various vegetation parameters, including biomass (Liu et al., 2015; Rodríguez-Fernández et al., 2018; Vittucci et al., 2018; Vittucci et al., 2019), LAI (Saleh et al., 2006; Saleh et al., 2007; Kerr et al., 2012; Kumar et al., 2020), NDVI (Jones et al., 2012; O'Neill et al., 2015), and canopy height (Vittucci et al., 2021; Li et al., 2022; Vittucci et al., 2023). Although the correlation coefficients of VOD with NDVI, LAI, and canopy height are comparable, VOD has a more linear relationship with LAI and height than with NDVI (Wigneron et al., 2017; Li et al., 2021). Compared with canopy height data, dynamic satellite LAI data are more easily obtained. Compared with NDVI, LAI provides clearer biophysical significance (Cao et al., 2023), as it is closely related to canopy structure and biomass. Since VWC (in kg m^{-2}) correlates with biomass (Xiao et al., 2016; Fang et al., 2019), LAI is likely a more suitable choice as prior information for VOD retrievals.

As mentioned earlier, the roughness parameter H_{rp} in the HQN model affects VOD retrieval significantly. Several studies have investigated the parameterization of surface roughness (Pan et al., 2014; Gao et al., 2020a; Konkathi and Karthikeyan, 2022). Initially, H_{rp} was linked to physical roughness characteristics like RMS height (s) and autocorrelation length (l) (Choudhury et al., 1979; Wigneron et al., 2001; Mialon et al., 2012; Lawrence et al., 2013). However, field measurements of these parameters are time-consuming (Martens et al., 2015) and site-specific, failing to adequately represent footprint-scale conditions. Parameter H_{rp} has also been modeled as a function of soil moisture, relying on the linear relationship between H_{rp} and soil moisture (Escorihuela et al., 2007; Saleh et al., 2007; de Jeu et al., 2009). This relationship is valid for sandy soils but not for heavy clay soils (Panciera et al., 2009; Martens et al., 2015). Moreover, the parameter H_{rp} exhibits significant temporal variability because it is influenced by weather events such as precipitation and strong winds, as well as agricultural activities like tillage (Zeng et al., 2016; Walker et al., 2019; Walker et al., 2023). To address these limitations, an empirical model was proposed to capture the dependence of the surface roughness parameter (H_{rp}) on roughness, soil moisture, and vegetation effects via TB and LAI (Martens et al., 2015; Wigneron et al., 2017). The authors noted that although this data-driven model lacks a physical basis, it is not site-specific as it accounts for diverse land cover and soil textures. Notably, the underlying multivariate nonlinear relationship remains unchanged—thus laying the foundation for cross-regional applicability. Additionally, validating this model is meaningful, given its readily available and consistent parameters, its potential to decouple the H_{rp}-SM dependence and further improve SM retrieval accuracy (Wigneron et al., 2017), and its ability to provide dynamic daily H_{rp}.

Field experiments are essential for developing, validating, and improving soil moisture and VOD retrievals. To address uncertainties in SMAP soil moisture retrievals, several Soil Moisture Active Passive Experiments (SMAPVEX) have been conducted across different regions, including North America and Canada (Colliander et al., 2012; Colliander et al., 2019). Using PALS observations, Colliander et al. (2019) found a deviation between measured VWC and NDVI climatology derived VWC in SMAP, particularly during the growing seasons. At the carman site, Colliander et al. (2019) identified that discrepancies in soil moisture retrievals were related to variations in vegetation and surface roughness. Therefore, the SMAPVEX-16 dataset from Carman provides an opportunity to validate the effectiveness of VOD with measured VWC and biomass, and to refine the retrieval strategy.

Therefore, this study aims to improve SMAP VOD retrieval by synergistically considering VOD and H_{rp}. This study attempts to answer the following questions: 1) Compared to constant H_{rp}, to what extent can the daily dynamic H_{rp} improve VOD retrieval across various inversion algorithms? 2) Compared to NDVI climatology, to what degree can measured LAI more effectively constrain VOD retrievals across various inversion algorithms? 3) How can we synergistically upscale field-based LAI and H_{rp} to improve satellite footprint-scale VOD retrieval? To address these questions, we utilize the dataset from the SMAPVEX16 field experiment conducted at Carman (SMAPVEX16-MB) to investigate these tasks. First, we calibrate H_{rp} by comparing four parameterization schemes across three inversion algorithms (MT-DCA, RDCA and CMCA). Based on the optimal H_{rp} parameterization, we evaluate two types of prior information—measured LAI and NDVI climatology—for VOD retrievals across the MT-DCA with constrained bounds (constrained MT-DCA, C-MT-DCA), as well as RDCA and CMCA. Measured LAI is considered effective prior information for VOD, as it reflects real-time vegetation status and is less prone to saturation. Finally, we investigate how to synergistically upscale field-based H_{rp} and LAI to satellite footprint scale to achieve applicability at the satellite pixel scale. This is mainly enabled by the similar passive signature between SMAP and PALS observations.

2. Materials

2.1. Study sites

The study area, located in southwestern Winnipeg, Carman, Canada, is characterized by intensive agriculture, with representative crops such as canola, soybeans, oats, and corn cultivated annually. It exhibits

significant variation in soil texture, ranging from sandy loam in the southwest to heavy clay in the northeast. Due to this diversity in soil and vegetation, several research initiatives, including the Soil Moisture Active Passive Validation Experiments (SMAPVEX12 and SMAPVEX16-MB), were conducted at this site. In SMAPVEX12, the study area spanned 13 × 70 km^2, covering 55 agricultural fields, while in SMAPVEX16-MB, the area was 26 × 48 km^2 and included 50 fields, each approximately 800 m by 800 m. The observations during the SMAPVEX12 and SMAPVEX16-MB campaigns comprised airborne L-band TB using PALS (Bhuiyan et al., 2018; Wang et al., 2021b), ground truth soil moisture measurements, and data on vegetation and surface roughness. Fig. 1 shows the locations of Carman and the distribution of manual sampling fields. Detailed descriptions can be seen in the studies of Colliander et al. (2016), McNairn et al. (2017), Bhuiyan et al. (2018), and Cosh et al. (2019).

2.2. Datasets

2.2.1. SMAPVEX12 and SMAPVEX16-MB

2.2.1.1. PALS brightness temperature. The PALS instrument is characterized by its ability to provide spatiotemporally coincident measurements from both a radiometer and a radar, with both sets of data acquired via the same antenna through a fast-switching sequence (Wilson et al., 2001; Colliander et al., 2015). PALS has previously been deployed in a range of soil moisture research efforts, as documented in studies by Njoku et al. (2002), Narayan, Lakshmi, and Njoku (2004), Bindlish et al. (2009), and Colliander et al. (2012), among others. For the SMAPVEX16-MB campaign, PALS was mounted on a DC-3 aircraft (Colliander et al., 2019), while for the SMAPVEX12 campaign, it was mounted on a Twin Otter aircraft (Colliander et al., 2015). The instrument facilitated a full 360° conical scan at a 40° incidence angle, consistent with the observing angle of SMAP. The arrangement in the SMAPVEX16-MB included high-altitude (3000 m) and low-altitude (1200 m) flight modes, producing ground footprints of 1500 m by 2000 m and 600 m by 800 m, respectively, with effective resolutions of about 1500 m and 600 m (derived from the square root of the footprint ellipse area). In contrast, the aircraft in the SMAPVEX12 flew at altitudes of 2750 m and 1200 m, producing ground footprints of 1330 m by 1780 m and 580 m by 780 m, respectively, with effective resolutions of about 1360 m/ 1400 m and 600 m (derived from the square root of the footprint ellipse area) (Colliander et al., 2015; McNairn et al., 2015). The TB obtained from the high-altitude flights covered the entire experimental domains, while those from the low-altitude flights encompassed portions of the domains, with effective resolutions aligning with typical field sizes in the area. The SMAPVEX16-MB campaign centered on two intensive observation periods (IOPs): June 8–20 and July 14–22, 2016, while SMAPVEX12 focused on an IOP from June 7 to July 19, 2012.

2.2.1.2. Soil parameters. Soil temperature and moisture measurements were taken along two parallel transects (200 m apart) for each field, with 16 evenly distributed sample points collected from June 7 to July 19, 2012, and from June 8 to July 22, 2016 (Bhuiyan et al., 2018; Wang et al., 2018). Soil temperature was recorded at 5 cm and 10 cm depths across four points using a digital pocket thermometer, while surface temperatures were measured with a thermal infrared thermometer in both sunlight and shade (McNairn et al., 2017). Soil moisture at a depth of 0–6 cm was determined with Stevens Hydra Probes (McNairn et al., 2015; McNairn et al., 2016; McNairn et al., 2017; Wang et al., 2018).

Surface roughness parameters such as *s* and *l*, were measured randomly at two of the 16 locations in each field with a 1-m mechanical profiler (McNairn et al., 2017). To obtain the 3-m profile, the instrument was moved twice to capture three consecutive 1-m profiles (Wang et al., 2021b).

2.2.1.3. Crop parameters. During the experimental periods from June 11 to July 18 in 2012, and from June 13 to July 21, 2016, various vegetation parameters (temperature, volumetric water content (M_v, m^3/m^3 or %), fresh and dry biomass, height, and LAI) were determined. Vegetation temperatures were measured concurrently in both sunlight and shade using a thermal infrared thermometer at the same plots where soil temperatures were recorded (McNairn et al., 2017). Destructive sampling provided data on crop height, biomass, and VWC. LAI was measured using digital hemispheric photographs, with 14 images captured along two transects at each of the three vegetation locations (McNairn et al., 2017).

2.2.2. Optical observations

Satellite-based optical indices, NDVI and LAI, were obtained at spatial resolutions of 30 m and 500 m, respectively. The 16-day NDVI was calculated from Landsat 8 Collection2 Level 2 Tier1 Surface Reflectance (LANDSAT/LC08/C02/T1_L2), while the 4-day LAI was derived from the MODIS MCD15A3H product. Following the method proposed by Bindlish et al. (2011), the 10-day NDVI climatology was generated using data from 2014 to 2023. Similarly, LAI climatology was derived using the same approach as for the NDVI climatology.

3. Methodology

3.1. Existing radiative transfer models and inversion algorithms

3.1.1. τ-ω model

The model has three components: i) upward soil emission attenuated by vegetation; ii) upward emission from vegetation; and iii) downward emission from vegetation, reflected by soil and further attenuated by vegetation. Therefore, the observed brightness temperature (TB_p) is simulated as follows:

$$TB_p = e_p\gamma_p T_s + (1-\omega_p)\left(1-\gamma_p\right)T_c + (1-\omega_p)\left(1-\gamma_p\right)T_c r_p \gamma_p \quad (1)$$

where T_s and T_c represent the effective temperatures of soil and canopy, respectively; ω_p refers to the effective scattering albedo of the canopy at *p* polarization; γ_p denotes the canopy transmissivity at *p* polarization; and e_p denotes the soil emissivity, which is derived from the soil reflectivity (r_p) using the equation $e_p = 1 - r_p$. Here, the subscript $p \in \{h, v\}$ represents horizontal (*h*) or vertical (*v*) polarization.

The canopy transmissivity γ_p is related to the vegetation optical depth (τ_p) through the following attenuation equation:

$$\gamma_p = e^{-\tau_p/\cos(\theta)} \quad (2)$$

where θ is the incidence angle and τ_p is assumed to be linearly proportional to the vegetation water content, with b_p as the linear coefficient (Jackson and Schmugge, 1991; Van de Griend and Wigneron, 2004a).

$$\tau_p = \tau_{NAD\_p}\left(tt_p sin^2\theta + cos^2\theta\right) \quad (3)$$

$$\tau_{NAD\_p} = b_p \times VWC \quad (4)$$

In this equation, with τ_{NAD_p} as the vegetation optical depth at nadir; and tt_p is the vegetation- and polarization-dependent parameter.

The reflectivity of rough soil (r_p) is empirically linked to the reflectivity of bare smooth soil (r_p/r_q, $p, q = h$ or v; $p \neq q$):

$$r_p = \left[(1-Q)\cdot r_{ps} + Q\cdot r_{qs}\right]\cdot e^{\left(-H_{rp}\cos^{N_p}(\theta)\right)} \quad (5)$$

where r_{ps} and r_{qs} are the *p*- and *q*-polarized specular reflectivity; N_p describes the soil roughness depending on the incidence angle (Colliander et al., 2016; Wigneron et al., 2017); and *Q* represents the effect of soil roughness on polarization mixing (Martens et al., 2015). The parameterization is provided in Section 3.1.3.

Table 1
Parameterizations of b, ω, Q, H_{rp} and N_p in the τ-ω model across three algorithms.

Algorithms	b	ω	Q	H_{rp}	N_p
RDCA	0.11	0.06	0.1771 H_r	Retrieval	2
MT-DCA	/	Retrieval	0	0.13	0
CMCA	0.11	0.05	0	0.12	2

3.1.2. Different inversion algorithms

MT-DCA, RDCA, and CMCA are three well-developed retrieval algorithms that can simultaneously retrieve SM and VOD (Konings et al., 2016; Konings et al., 2017; Ebtehaj and Bras, 2019; Chaubell et al., 2020; Chaubell et al., 2021; Gao et al., 2021). Below is a concise overview of these algorithms.

3.1.2.1. Regularized dual channel algorithm (RDCA). A regularization term for VOD is incorporated into the classic DCA to reduce spatio-temporal noise during the retrieval process. Details of this algorithm can be found in Chaubell et al. (2020), O'Neill et al. (2020), and Chaubell et al. (2021).

$$\min_{SM,VOD} J(Y) = \left(e_p^{obs} - e_p^{sim}\right)^2 + \lambda(VOD - VOD^*)^2 \tag{6}$$

where e_p^{obs} and e_p^{sim} are the observed and simulated soil surface emissivity, respectively; e_p^{obs} is calculated as TB_p/T_s; the regularization parameter λ is set to 2 via the combination of a searching method and a cross-validation method—a common approach used in the passive microwave retrieval algorithms (Ebtehaj and Bras, 2019; O'Neill et al., 2020; Gao et al., 2021); and VOD^* is the initial estimate of VOD calculated from NDVI climatology.

3.1.2.2. Multi-temporal dual channel algorithm (MT-DCA). The MT-DCA leverages emissivity observations from at least two consecutive overpasses, typically spanning one week. This algorithm assumes that VOD remains constant, while SM changes temporally within this time frame (Konings et al., 2016; Konings et al., 2017).

$$\min_{SM_t,VOD} J(Y) = \sum_{t=0}^{T} \left(e_{pt}^{obs} - e_{pt}^{sim}\right)^2 \tag{7}$$

where $SM_t = (SM_1, \ldots, SM_t)$. When three overpasses are available per pixel, the algorithm enables the simultaneous retrieval of parameter ω, SM, and VOD.

3.1.2.3. Constrained multi-channel algorithm (CMCA). The CMCA incorporates Tikhonov (Tikhonov, 1963) and Sobolev-norm regularization (Adams and Fournier, 2003) terms into the MT-DCA to consider gradual temporal changes in VOD and mitigate the ill-conditioning of the retrieval problem caused by highly correlated polarized emissivity (Eq. (8)) (Ebtehaj and Bras, 2019). Simultaneously, the estimation of SM and VOD is constrained within their reliable bounds using box-constrained least-squares methods (Sorensen, 1982; Celis et al., 1984; Byrd et al., 1987). For more details, see Ebtehaj and Bras (2019).

$$\begin{aligned} &\min_{SM_t,VOD_t} J(Y) = \sum_{t=0}^{T} \left(e_{pt}^{obs} - e_{pt}^{sim}\right)^2 + \lambda(D_1\gamma_t)^2 \\ &subject\ to\ SM_t^l \le SM_t \le SM_t^u,\ \ VOD_t^l \le VOD_t \le VOD_t^u \end{aligned} \tag{8}$$

where $SM_t = (SM_1, \ldots, SM_t)$ and $VOD_t = (VOD_1, \ldots, VOD_t)$; λ is the regularization parameter, with a suggested value of 50 determined by the combination of searching method and cross-validation method mentioned above (Ebtehaj and Bras, 2019; O'Neill et al., 2020; Gao et al., 2021); D_1 is the first discrete derivative operator; and the retrieval bounds are defined as the lower (l) and the upper (u) bounds. The bounds of SM are based on the wilting point and field capacity for various soil types, while the VOD bounds are derived from MODIS NDVI climatology, utilizing the linear relationship between VOD and VWC (Chan et al., 2013).

3.1.3. Parameterization for the retrieval algorithms

PALS TB (with a spatial resolution of 600 m) is used to retrieve VOD. The mean TB for each field is calculated by averaging values from the footprint center within 150 m of the field center. Through this method, the PALS footprints showing the highest overlap with a particular field are chosen to estimate a representative TB for that field (Colliander et al., 2016; Wang et al., 2021b). The effective soil temperature is determined by averaging 5-cm-depth and the surface soil temperatures (accounting for both sunlight and shade conditions) (Colliander et al., 2015; Wang et al., 2021b), while the effective canopy temperature is assumed to be equal to it based on soil-canopy thermal equilibrium (Colliander et al., 2016; Colliander et al., 2019). Theoretically, the effective soil temperature depends on surface/deep soil temperature and soil moisture (Choudhury et al., 1982; Wigneron et al., 2017; O'Neill et al., 2020). The SMAP algorithms typically use a modified formulation of the Choudhury model, in which the soil moisture effect is included in a calibrated fixed parameter C (O'Neill et al., 2020). However, the exact physical temperature distribution in soils is difficult to obtain. The soil-canopy thermal equilibrium assumption is adopted by SMOS/SMAP official algorithms at 6:00 AM/PM. Theoretically, this assumption is most robust at 6:00 AM due to weak canopy transpiration and more vertically uniform soil temperature/dielectric property profiles (Fagerlund et al., 1970; Basharinov and Shutko, 1975; O'Neill et al., 2020). Notably, this study's measurements were conducted in the early morning or early evening, avoiding midday and drought periods to minimize thermal equilibrium violations caused by temperature heterogeneity from extreme radiative forcing. Though this simplification deviates from basic energy balance principles, it has been adopted in retrieval studies using SMOSREX and SMAPVEX datasets (Wigneron et al., 2004; Saleh et al., 2006; Schlenz et al., 2012; Colliander et al., 2015; Colliander et al., 2019), mainly because precise vertical-spatial temperature profiles of soil and vegetation are hard to measure in the field. Additionally, we tested an alternative, widely used parameterization for effective canopy temperature (i.e., averaging sunlit and shaded canopy temperatures) (Pardé et al., 2003; Colliander et al., 2012; McNairn et al., 2015; Colliander et al., 2016). This method yielded VOD retrievals consistent with the thermal equilibrium assumption, mainly because the temperature difference between this average and the soil temperature average is small—introducing minimal error in surface reflectivity (Colliander et al., 2012; McNairn et al., 2015).

The reflectivity of bare, smooth soil is calculated using Fresnel equations and the Mironov dielectric model (Njoku and Entekhabi, 1996; Mironov et al., 2009; Mironov et al., 2017). The parameter tt_p is set to one, assuming that vegetation behaves isotropically with respect to microwave propagation. In fact, tt_p is theoretically vegetation-type specific and exhibits seasonal differences or temporal changes due to structural changes in vegetation (Pardé et al., 2003; Wigneron et al., 2004; Peischl et al., 2012; Schwank et al., 2012; Yan et al., 2015; Wigneron et al., 2017). To ensure a fair comparison of the three algorithms and reduce their degree of freedom (Konings et al., 2015), all algorithms use field-averaged in-situ soil moisture measurements as input. Regularization parameters in the RDCA and CMCA are calibrated based on experimental data via the combination of a searching method and a cross-validation method mentioned above (Adagbasa et al., 2019; Ebtehaj and Bras, 2019; O'Neill et al., 2020; Ghorbanzadeh et al., 2020; Gao et al., 2021). Additionally, the parameterizations of b, ω, Q, H_{rp} and N_p vary across retrieval algorithms, but these algorithms assume them to be independent of polarization (Konings et al., 2016; Konings et al., 2017; Ebtehaj and Bras, 2019; O'Neill et al., 2020), as shown in Table 1. Theoretically, these five parameters depend on polarization and exhibit temporal changes (Van de Griend and Wigneron, 2004b; Lawrence et al., 2013; Martens et al., 2015; Wigneron et al., 2017), but this assumption

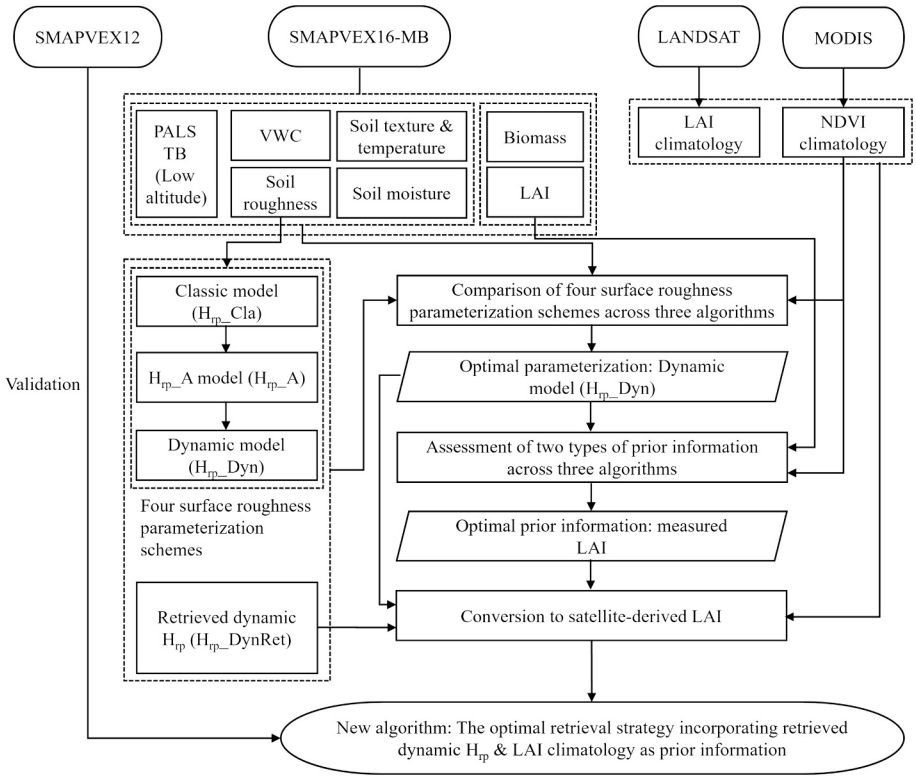

Fig. 2. Flow chart presenting the retrieval algorithm of VOD from PALS data (The process consists of three main steps: 1) Assessment of four H_{rp} parameterization schemes across three algorithms; 2) Evaluation of two types of prior information across three algorithms; 3) Synergistic upscaling of field-based H_{rp} and LAI to satellite footprint-scale to achieve applicability at the SMAP pixel scale.)

Table 2
Coefficient values of dynamic H_{rp} model (Eq. (9)).

LAI	Coefficients							
	c_{1h}	c_{2h}	c_{3h}	c_{4h}	c_{1v}	c_{2v}	c_{3v}	c_{4v}
0–2	−1.28	0.0096	2	−0.13	−3.69	0.0181	2	−0.08
2–3	−1.36	0.0108	2	−0.2	−3.19	0.0168	2	−0.14
3–4	−1.58	0.0117	2	−0.18	−4.57	0.0214	2	−0.09
4–6	−1.44	0.0141	2	−0.34	−3.6	0.022	2	−0.35

This table refers to Martens et al. (2015).

remains commonly used. This is because there is currently a lack of reference standards for their parameterizations across various crops. In RDCA and CMCA, VWC is calculated from NDVI climatology using Landsat data from 2014 to 2023, as detailed in Section 3.2.2. The LAI climatology is generated in the same manner as the NDVI climatology (Bindlish et al., 2015). Unless specified otherwise, all parameters in this study follow the parameterizations outlined above.

3.2. Improvement of VOD retrieval algorithm

Fig. 2 presents the development of the new algorithm using PALS data from the SMAPVEX16-MB dataset. We first compare four parameterization schemes, including three H_{rp} models and the original algorithm parameterization across three well-developed retrieval algorithms: MT-DCA, RDCA, and CMCA. Two models rely on geometric characteristics, typically measured once due to measurement difficulties, while one dynamic model incorporates microwave observations and vegetation information for daily updates (Choudhury et al., 1979; Lawrence et al., 2013; Martens et al., 2015). This dynamic model is theoretically optimal for capturing H_{rp} changes from agricultural practices and weather. During H_{rp} tuning, we compare the Pearson correlation coefficient (R) of different parameterization schemes between VOD retrievals and VWC/biomass to screen for the most effective parameterization scheme. This tuning method leverages the well-established correlation between VOD and VWC/biomass (Jackson and Schmugge, 1991; Pardé et al., 2003; Van de Griend and Wigneron, 2004a), aligning with algorithm development, improvement, and validation in previous studies (Martens et al., 2015; Colliander et al., 2019; Wang et al., 2021a; Wang et al., 2021b). This tuning method is mainly justified because VOD and H_{rp}, as radiative transfer parameters, cannot be directly measured in situ (Wigneron et al., 2017; Li et al., 2021). As a critical premise for this method, this linear relationship between VOD and VWC/biomass is stable, driven by the intrinsic physical mechanism of "VWC-driven microwave attenuation". Notably, this linear relationship is unaffected by the above retrieval algorithms because the retrieval constraints in these algorithms solely optimize parameter inversion stability (without altering the physical mechanism). Comparing these three algorithms (MT-DCA, RDCA, and CMCA) also helps identify their strengths, weaknesses, and improvement potentials.

Based on the optimal H_{rp} parameterization, we evaluate in-situ measured LAI and NDVI climatology as prior information across RDCA, C-MT-DCA, and CMCA. C-MT-DCA (MT-DCA with constrained bounds like CMCA) may enhance retrieval precision and help assess the effectiveness of prior information. Consistent with the H_{rp} tuning method, we screen candidate prior information by evaluating the correlation between VOD retrievals and VWC/biomass, and further verify its validity using the correlation between the prior information and VWC/biomass. LAI is a more reasonable indicator for constraining VOD, as it directly reflects vegetation growth, photosynthetic capacity, canopy structure, and biomass, all closely linked to VWC (Xiao et al., 2016; Fang et al., 2019).

To scale up the retrieval approach, measured LAI will be replaced with satellite-derived LAI climatology. Once LAI and H_{rp} are upscaled to satellite-derived data, the algorithm can be applied to SMAP, given the consistent passive signature between PALS and SMAP observations. In

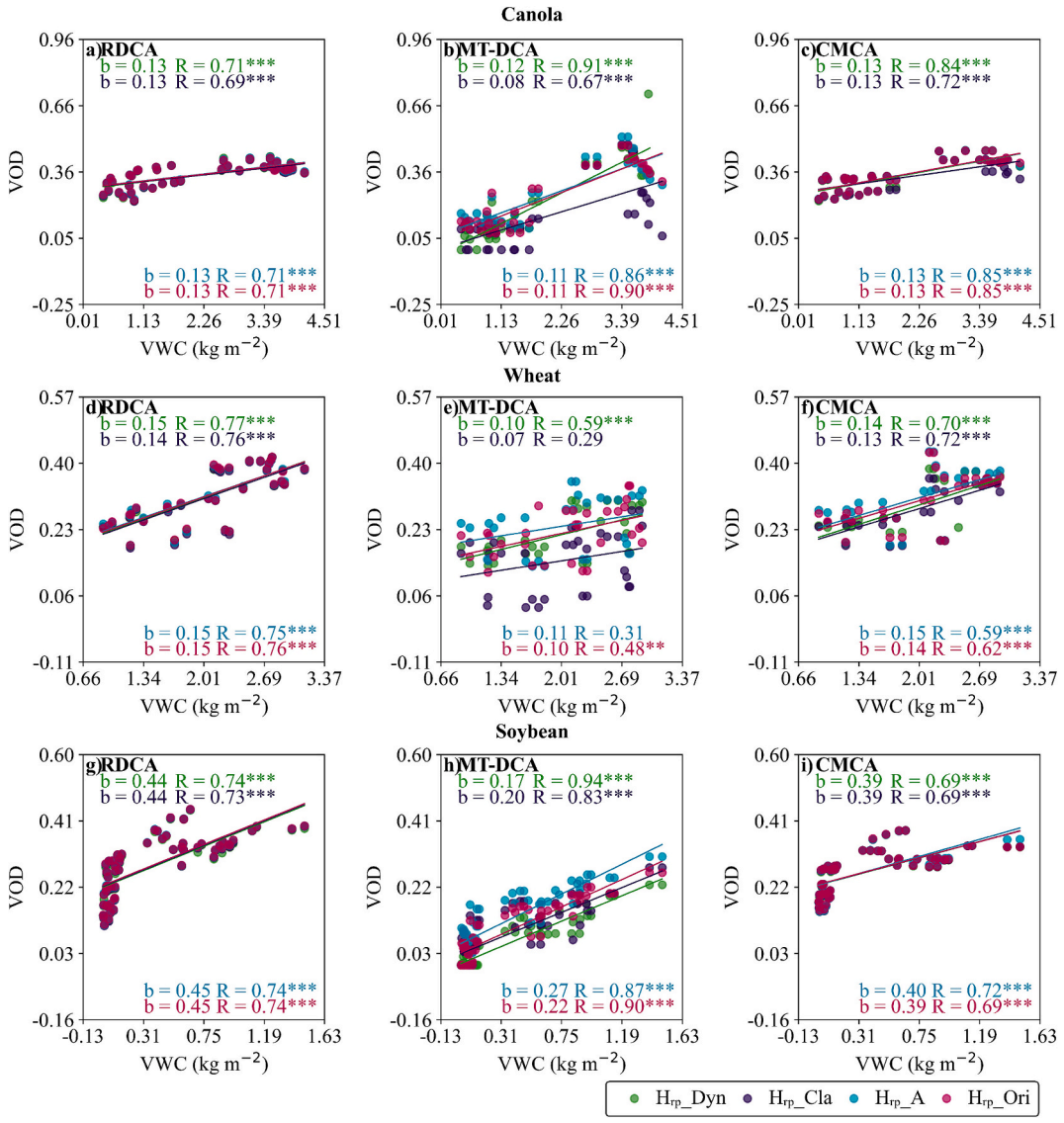

Fig. 3. The correlations between VWC and VOD retrieved from RDCA, MT-DCA, and CMCA, using four H_{rp} parameterizations (H_{rp}*_DynMes*, H_{rp}*_Cla*, H_{rp}*_A* and H_{rp}*_Ori*). H_{rp}*_DynMes* represents the H_{rp} derived from the H_{rp}*_Dyn* model with in-situ measured LAI input. Parameter *b* is the slope of the zero-intercept linear regression between VOD and VWC. ** and *** represent statistical significance at the 0.01 and 0.001 significance levels (i.e., $P < 0.01$ and $P < 0.001$), respectively.

this process, the improved algorithm is selected primarily based on the correlation between VOD and VWC/biomass. A supplementary validation is conducted using the R and root mean squared error (RMSE) between forward-simulated TB (input with VOD retrievals) and observed TB—an approach widely used in passive microwave retrieval studies (Martens et al., 2015; Colliander et al., 2016; Colliander et al., 2019; Wang et al., 2021b). Finally, the improved algorithm is independently validated using the SMAPVEX12 dataset. Notably, though real-time dynamic LAI is more accurate for capturing vegetation responses to climate extremes, it is rarely observed at the field scale (typically 800 m) during the observation days of SMAPVEX16-MB. Future studies will explore the impact of real-time dynamic LAI on VOD retrievals for SMAP retrievals.

3.2.1. *Four parameterization schemes for effective roughness parameter*

Four parameterization schemes are evaluated, which include three models representing two distinct strategies for H_{rp} calculation (Eqs. (9)–(12)) and the parameterization scheme from the original algorithm (H_{rp}*_Ori*; Table 1). The three models are as follows:

1) One of the models is an empirical model proposed by Martens et al. (2015) and referred to as the dynamic H_{rp} model (H_{rp}*_Dyn*) (Eq. (9)), which characterizes a dynamic roughness parameter that depends on polarization. This model links roughness to TB and LAI and can provide daily parameter values, showing potential for large-scale application. In this study, two variants of H_{rp} derived from this model are distinguished by LAI data sources: H_{rp}*_DynMes* (calculated with in-situ measured LAI) and H_{rp}*_DynSat* (using satellite-derived LAI climatology), with the latter used in subsequent Sections 3.2.3 and 4.3.

$$H_{rp}\_Dyn = \left(c_{1p} + c_{2p}TB_p + c_{4p}LAI\right)^{c_{3p}} \tag{9}$$

where the values of c_{1p}, c_{2p}, c_{3p} and c_{4p} are taken from Martens et al. (2015) (Table 2).

2) The second model, proposed by Choudhury et al. (1979) and termed the classic H_{rp} model (H_{rp}*_Cla*), relates H_{rp} to *s* (Eq. (10)) and is insensitive to microwave frequency (Montpetit et al., 2015).

$$H_{rp}\_Cla = 4k^2s^2 \tag{10}$$

3) Another model, developed by Lawrence et al. (2013) and referred to as H_{rp}*_A*, links H_{rp} to physical surface roughness characteristics such as *s* and *l* (Eqs. (11)–(12)). H_{rp}*_A* is one of six models (A-F) sharing the same

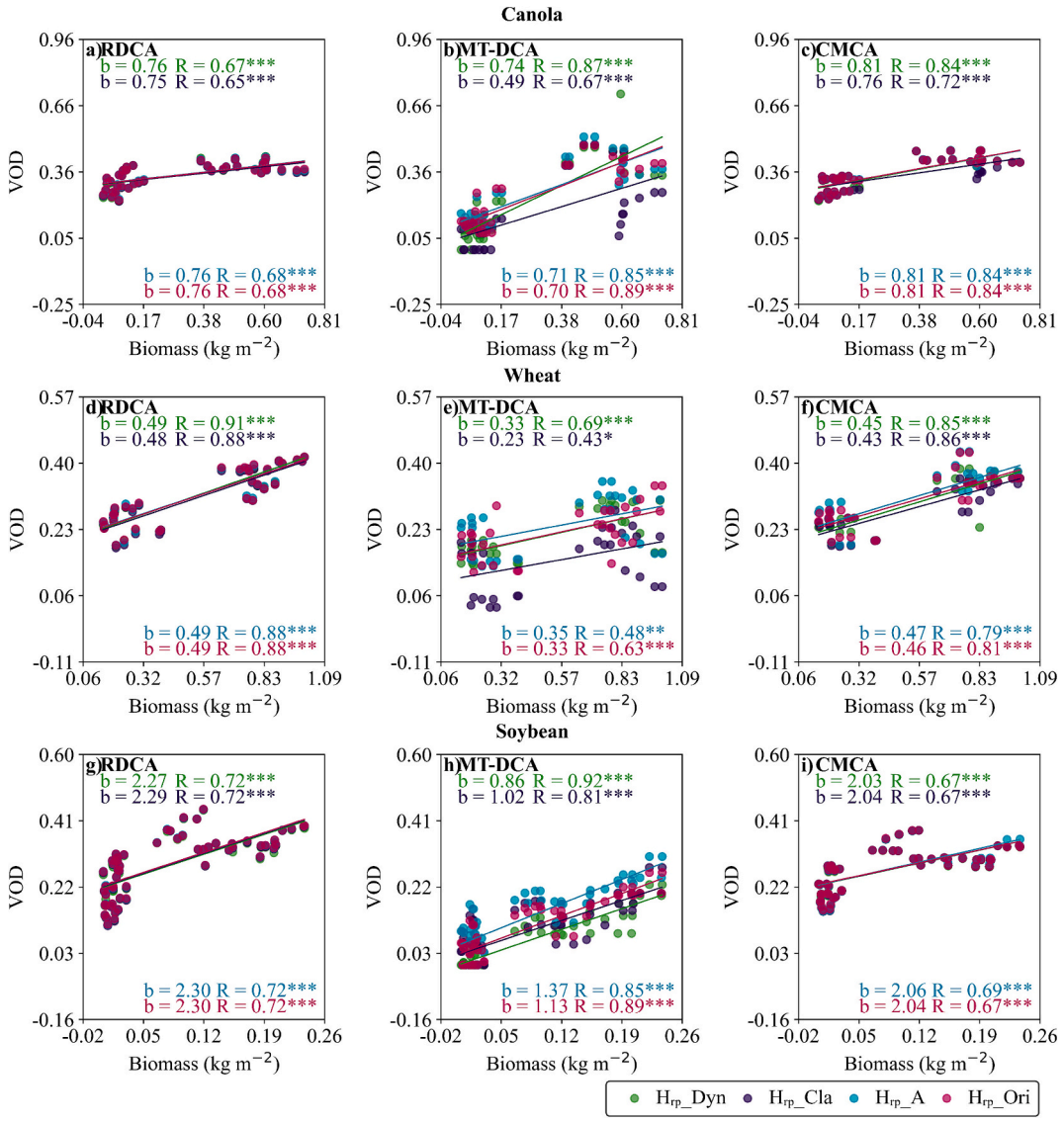

Fig. 4. The correlations between biomass and VOD retrieved from RDCA, MT-DCA, and CMCA, using four H_{rp} parameterizations (H_{rp}*_DynMes*, H_{rp}*_Cla*, H_{rp}*_A* and H_{rp}*_Ori*). H_{rp}*_DynMes* represents the H_{rp} derived from the H_{rp}*_Dyn* model with in-situ measured LAI input. Parameter *b* is the slope of the zero-intercept linear regression between VOD and biomass. *, **, and *** represent statistical significance at the 0.05, 0.01 and 0.001 significance levels (i.e., $P < 0.05$, $P < 0.01$, and $P < 0.001$), respectively.

exponential function structure and exhibiting similar trends in the retrieved parameters. H_{rp}*_A* shows a slightly lower RMSE between TB simulated by the HQN model and that observed by the PORTOS radiometer, as well as between retrieved and measured soil moisture. Moreover, the z_s parameter demonstrates a stronger correlation with the radar backscattering coefficient than the *s* parameter (Zribi et al., 2014).

$$H_{rp}\_A = 2.651\left(1 - e^{-Z_s/2.473}\right) \tag{11}$$

$$Z_s = s^2/l \tag{12}$$

3.2.2. Two types of vegetation indicators as prior information

Based on the optimal H_{rp} parameterization, we evaluate the performance of both in-situ measured LAI and NDVI climatology across RDCA, CMCA, and C-MT-DCA. In the two SMAP algorithms (RDCA and CMCA), VOD is constrained by VWC from the NDVI climatology (Eq. (13)) and the *b* values obtained from the IGBP land cover-based lookup table (Jackson, 1993; Bindlish et al., 2015).

$$VWC = 1.9134NDVI^2 - 0.3215NDVI + StemFactor\frac{NDVI_{max} - NDVI_{min}}{1 - NDVI_{min}} \tag{13}$$

where $NDVI_{max}$ and $NDVI_{min}$ represent the annual maximum and minimum NDVI values, respectively. According to the SMAP official algorithm, for croplands the current NDVI is used for $NDVI_{max}$ (O'Neill et al., 2020), consistent with the NDVI applied in the first two terms. The default $NDVI_{min}$ value for croplands in the SMAP algorithm is set to 0.1 (O'Neill et al., 2020). The stem factor in the SMAP algorithm signifies the maximum amount of water that can be stored in the stems of crops, and it is assigned a value of 3.5 (O'Neill et al., 2020).

In the SMOS L2 & L3 algorithms, VOD is initialized with a first guess derived from LAI and b' (Eq. (14)). It is noted that b' in Eq. (14) differs physically from the *b* used to generate the initial guess for VOD via Eq. (13).

$$\tau_{NAD} = b' \cdot LAI + b'' \tag{14}$$

where parameters b' and b'' are set to 0.06 and 0, respectively.

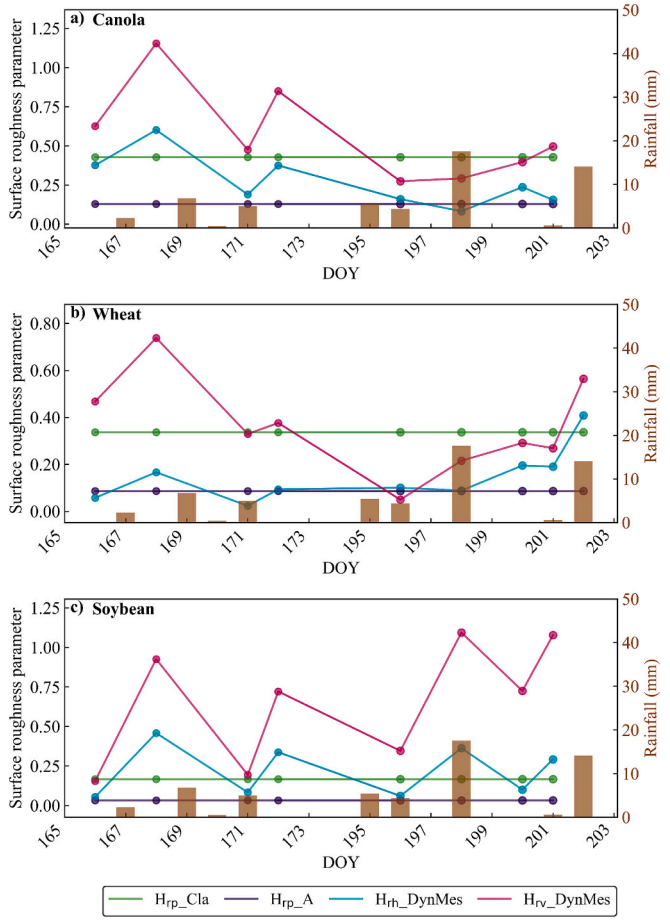

Fig. 5. Parameterization schemes for surface roughness parameter H_{rp} from three models and rainfall during SMAPVEX16-MB. H_{rh}*_DynMes* and H_{rv}*_DynMes* represent the H_{rp} at p polarization derived from the H_{rp}*_Dyn* model with in-situ measured LAI input.

The operational SMOS Level 2 algorithm uses typical b' values for low vegetation like croplands, with b'' set to 0 for simplicity (Martens et al., 2015). Actually, b' and b'' vary with vegetation type. For example, Schlenz et al. (2012) found that $b' = 0.12$ and $b'' = 0.08$ for SMOS when LAI constrains VOD. In contrast, for SMAP official algorithms, parameter b typically ranges around 0.12 (±0.03) across vegetation types (Jackson and Schmugge, 1991; Van de Griend and Wigneron, 2004b; Wigneron et al., 2017).

Theoretically, VOD retrieval can be influenced by temporal variations in LAI or NDVI climatology, as b' and b are generally assumed constant and b'' is set to 0. Hence, b' and b function in a similar manner in VOD retrieval and are thus uniformly referred to as b for convenience. Based on b values from 0.06 to 0.12 in previous studies, we test parameterizing b (0.06, 0.09 and 0.12) with LAI as prior information, setting b'' to 0. For CMCA, considering the high accuracy of field-measured LAI, we evaluate 10% and 15% multiplicative errors. For NDVI climatology, following the CMCA, we apply a 15% multiplicative error (Ebtehaj and Bras, 2019). Additionally, when using NDVI climatology to constrain VOD, the b values are prescribed according to the original algorithms (Table 1).

3.2.3. Upscaling field-based H_{rp} and LAI to satellite footprint scale

As anticipated, using dynamic H_{rp} parameterization and LAI as prior information will form the foundation for improving VOD retrieval. If b values do not significantly affect VOD retrieval, we set b to 0.10 within its common range of 0.06 to 0.12 (Van de Griend and Wigneron, 2004a; Saleh et al., 2006; Wigneron et al., 2007; Kerr et al., 2012; Schlenz et al., 2012; Lawrence et al., 2014; Ebtehaj and Bras, 2019; O'Neill et al., 2020), when using b and LAI to constrain VOD. Notably, due to the model's insufficient robustness and inherent errors in satellite-derived LAI, its direct application for upscaling H_{rp} and LAI to satellite-derived data may yield limited performance. To address uncertainties in the dynamic H_{rp} model and satellite-derived LAI climatology, as well as their complex interactions during VOD retrieval, we employ two methods to calculate dynamic H_{rp}: 1) using the dynamic H_{rp} model with satellite-derived LAI climatology input (H_{rp}*_DynSat*); 2) inverting from the τ-ω model with VOD determined by LAI and averaging the retrieved dynamic H_{rp} from two or three consecutive observations within a week (H_{rp}*_DynRet*). The latter adopts the H_{rp} upscaling strategy consistent with the SMAP official RDCA algorithm (Chaubell et al., 2020; O'Neill et al., 2020). This method incorporates H_{rp} as a co-optimization variable directly into the inversion process, theoretically completely avoiding the reliance on external empirical dynamic models such as Eq. (9). If the designed scheme performs as expected, the SMAPVEX12 dataset can serve as an independent validation dataset for the improved algorithm in this study.

We also explore the effects of NDVI climatology as prior information under both dynamic H_{rp} parameterizations: H_{rp}*_DynSat* and H_{rp}*_DynRet*. Because satellite-derived vegetation indicators interact with H_{rp} during VOD retrieval, complicating the identification of the best option. Additionally, we test a wide range of constraint bounds in C-MT-DCA and CMCA, applying a 20%–50% multiplicative error in 10% increments, and an additional 15% error for NDVI climatology following the CMCA.

3.3. Impact of input parameter uncertainties on VOD retrievals

To estimate the uncertainty of VOD retrieval, we employ the stochastic perturbation experiment and the τ-ω forward model, with a 5% perturbation applied to three input parameters (Colliander et al., 2012; Colliander et al., 2019): SM, LAI, and T_s. The stochastic perturbation experiment is a classical method for quantifying parameter sensitivity and evaluating model anti-interference ability, and has been widely used in fields such as remote sensing retrieval and numerical simulation (Xu et al., 2019; Ye et al., 2024; Shen et al., 2025).

We use the relative sensitivity coefficient (S, Eq. (15)) to quantify the response of VOD retrievals to unit perturbations of input parameters. To further analyze the perturbation effects, we calculate the R and RMSE between retrieved VOD values under two scenarios: perturbed and unperturbed.

$$S = (\Delta VOD / VOD_0)/(\Delta X / X_0) \tag{15}$$

where VOD_0 and X_0 denote the retrieved VOD and input parameter value under unperturbed (baseline) conditions, respectively; $\Delta VOD = VOD_{post\text{-}perturbation} - VOD_0$ represents the difference between post-perturbation and baseline VOD, and $\Delta X = X_{post\text{-}perturbation} - X_0$ represents the difference between post-perturbation and baseline parameter values.

4. Results and discussions

4.1. Comparison of different soil roughness parameter parameterizations

Figs. 3–4 summarize the correlations between VWC/biomass and VOD retrieved from RDCA, MT-DCA, and CMCA, using four H_{rp} parameterizations. The three algorithms exhibit a linear VOD-VWC/biomass correlation, while different H_{rp} parameterizations do not alter this relationship. For the same H_{rp} parameterization, although the zero-intercept regression slopes (parameter b) of VOD versus VWC show cross-algorithm differences for the same crop, they generally fall in a similar order of magnitude—all within the crop-specific range (0.05–0.45) reported (Saleh et al., 2006; Wigneron et al., 2017; O'Neill et al., 2020; Li et al., 2021; Wang et al., 2021b). Overall, RDCA produces higher VOD-VWC slopes for the same crop, while CMCA's slopes are very

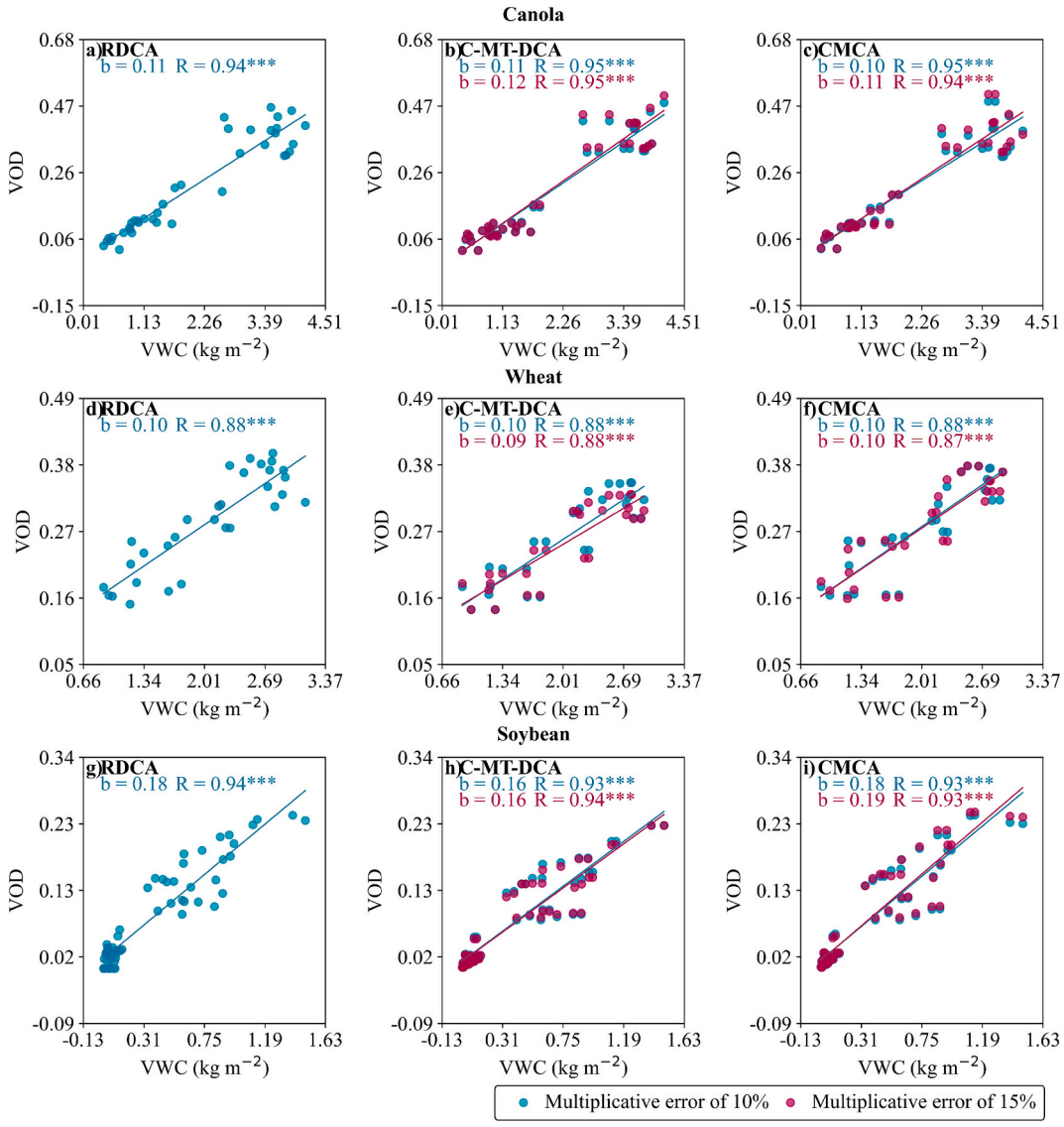

Fig. 6. The correlations between VWC and VOD retrieved from RDCA, C-MT-DCA with constraint bounds, and CMCA, using measured LAI as prior information for VOD with a b value of 0.09 and the dynamic H_{rp} model. Parameter b is the slope of the zero-intercept linear regression between VOD and VWC. *** represents statistical significance at the 0.001 significance level ($P < 0.001$).

close to these higher values for all crops. In contrast, MT-DCA has lower slope values than RDCA and CMCA.

The dynamic H_{rp} model (H_{rp}_DynMes) outperforms other models (H_{rp}_A and H_{rp}_Cla) or the parameterization in the original algorithms (H_{rp}_Ori), particularly in improving the correlation between VOD from MT-DCA/CMCA and VWC/biomass for wheat with complex structure. This superiority stems from three main factors. First, the dynamic model accounts for dielectric properties and vegetation effects across diverse land covers and soil textures (Martens et al., 2015). In contrast, the other two models rely solely on surface geometry, neglecting these effects (Choudhury et al., 1979; Lawrence et al., 2013; Martens et al., 2015). Notably, H_{rp} is determined by surface geometry when soil is saturated. However, as soil dries, water is retained in preferential locations, resulting in a heterogeneous water distribution and variations in soil dielectric properties, increasing soil dielectric roughness without changing physical roughness (Martens et al., 2015).

Second, the dynamic model considers polarization and dynamic characteristics. H_{rp} is theoretically dependent on polarization and dynamic changes caused by weather and agricultural activities (Escorihuela et al., 2007; Lawrence et al., 2013; Martens et al., 2015; Zeng et al., 2016; Walker et al., 2019; Walker et al., 2023), while geometric parameters are typically measured only once and are difficult to monitor over time. Observed polarization differences and dramatic H_{rp} fluctuations during crop growth suggest that assuming constant surface roughness fails to capture significant changes, impacting VOD retrieval (Fig. 5). Notably, no straightforward correlation between H_{rp} and individual rainfall events is observed in Fig. 5. This is because the dynamics of H_{rp} represent an integrated effect of multiple factors. In agricultural regions, farming activities (e.g., tillage) are typically the dominant driver (Zobeck and Onstad, 1987; Walker et al., 2019; Walker et al., 2023), exerting a greater influence than weather variations. Although heavy rainfall can alter bare soil roughness (Abban et al., 2017), its direct impact on H_{rp} is significantly attenuated under vegetation cover due to canopy shielding. Moreover, the influence of precipitation is intricately coupled with simultaneous changes in SM and VWC within the radiometric signal, making it challenging to isolate in either physical or retrieval terms (Colliander et al., 2016; Feldman et al., 2018). Therefore, due to the reasons outlined above, the dynamic variations of H_{rp} in vegetated areas do not exhibit a clear empirical relationship with individual rainfall events, which is consistent with existing

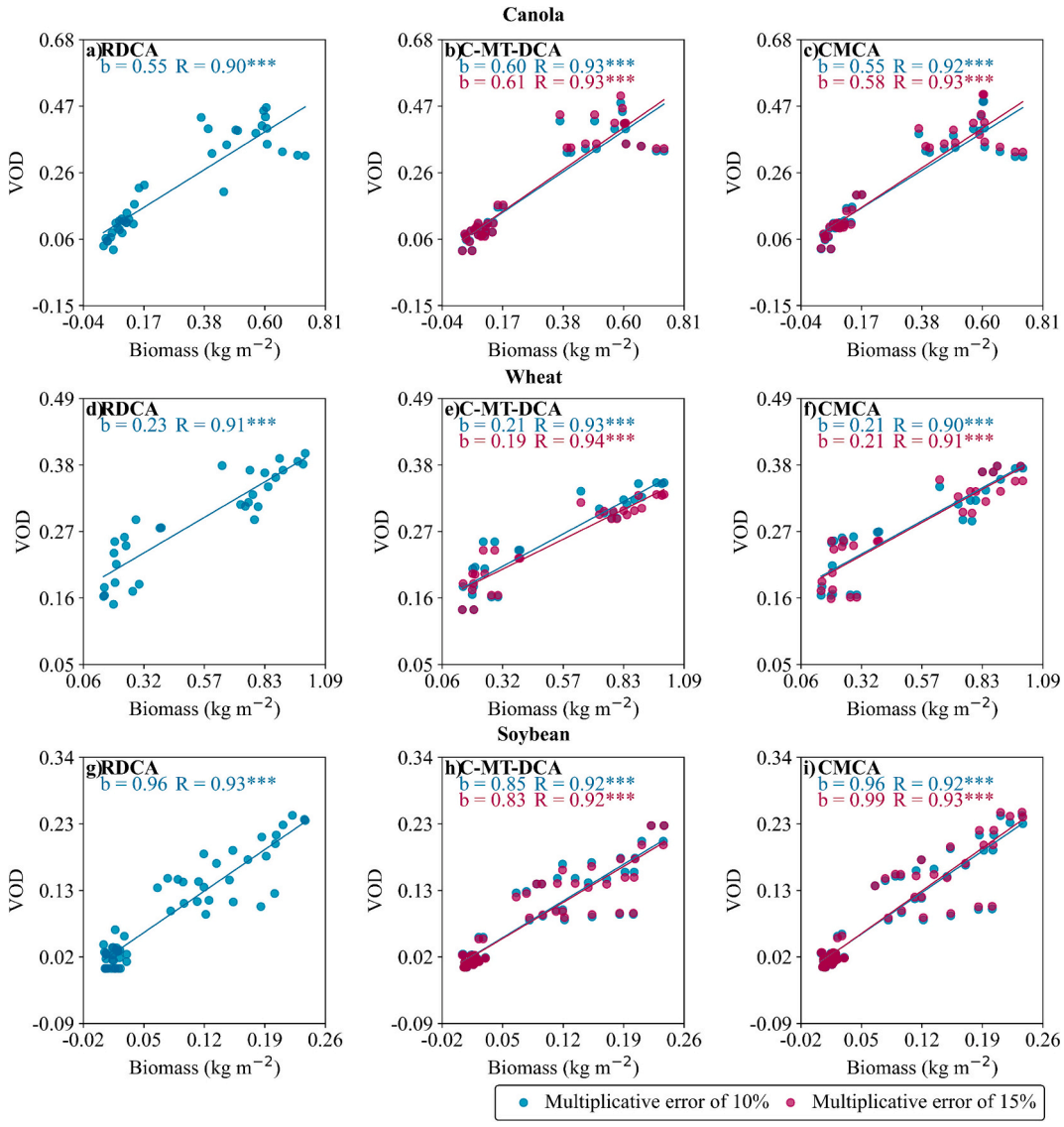

Fig. 7. The correlations between biomass and VOD retrieved from RDCA, C-MT-DCA with constraint bounds, and CMCA, using measured LAI as prior information for VOD with a b value of 0.09 and the dynamic H_{rp} model. Parameter b is the slope of the zero-intercept linear regression between VOD and biomass. *** represents statistical significance at the 0.001 significance level ($P < 0.001$).

understanding (Colliander et al., 2016; Walker et al., 2019; Walker et al., 2023; Feng et al., 2025).

Finally, surface geometric parameters reflect only the sampling location, not the pixel-covered area average. In contrast, H_{rp} from the dynamic model uses the average information of the entire pixel, making it more representative. Similarly, the parameterization in the original algorithms also faces the aforementioned issues. For example, MT-DCA and CMCA prescribe a single empirical H_{rp} constant value for both polarizations based on land cover, calibrated from early numerical or field experiments (Konings et al., 2017; Ebtehaj and Bras, 2019; Chaubell et al., 2020; O'Neill et al., 2020). RDCA retrieves H_{rp} from the τ-ω model as a constant for both polarizations, with VOD determined by NDVI climatology (Chaubell et al., 2020). Additionally, H_{rp}_A outperforms H_{rp}_Cla, consistent with Wang et al. (2021b). Specifically, by incorporating l in addition to s, H_{rp}_A simultaneously captures both the height variation characteristics and spatial continuity of the surface. This possibly mitigates the issue of H_{rp}_Cla: relying solely on s, H_{rp}_Cla tends to overestimate roughness as s increases under intermediate or strong roughness conditions (i.e., when $s >$ about 10 mm) (Wigneron et al., 2011). In SMAPVEX16-MB, s ranges from 0 to 20 mm (Wang et al., 2021b), where H_{rp}_Cla's overestimation bias may thus be pronounced.

It should be noted that the results demonstrate the application potential of the direct implementation of the empirical model combined with high-quality in-situ measurements for improving VOD retrieval accuracy in the SMAPVEX16-MB study area. However, the robustness of such empirical relationships (e.g., Eq. (9)) and their transferability to different geographical regions, ecosystems or spatial scales still require thorough validation with more extensive independent datasets.

In Figs. 3–4, MT-DCA exhibits the highest sensitivity to H_{rp}, followed by CMCA and then RDCA, aligning with the retrieval strategies. Generally, constraint boundaries provide physical limits, while regularization enhances flexibility and stability. Therefore, VOD retrieval in RDCA and CMCA is less influenced by H_{rp}. In RDCA, the regularization term based on NDVI climatology provides a stronger constraint, making the retrieval relatively independent of H_{rp} but strongly dependent on prior information. By contrast, the regularization term in CMCA, based on gradual VOD changes, serves as a weaker and more flexible constraint. Although CMCA uses NDVI climatology as a box constraint for VOD, its overall constraint may be weaker than that of RDCA. Compared with them, MT-DCA only assumes that VOD remains

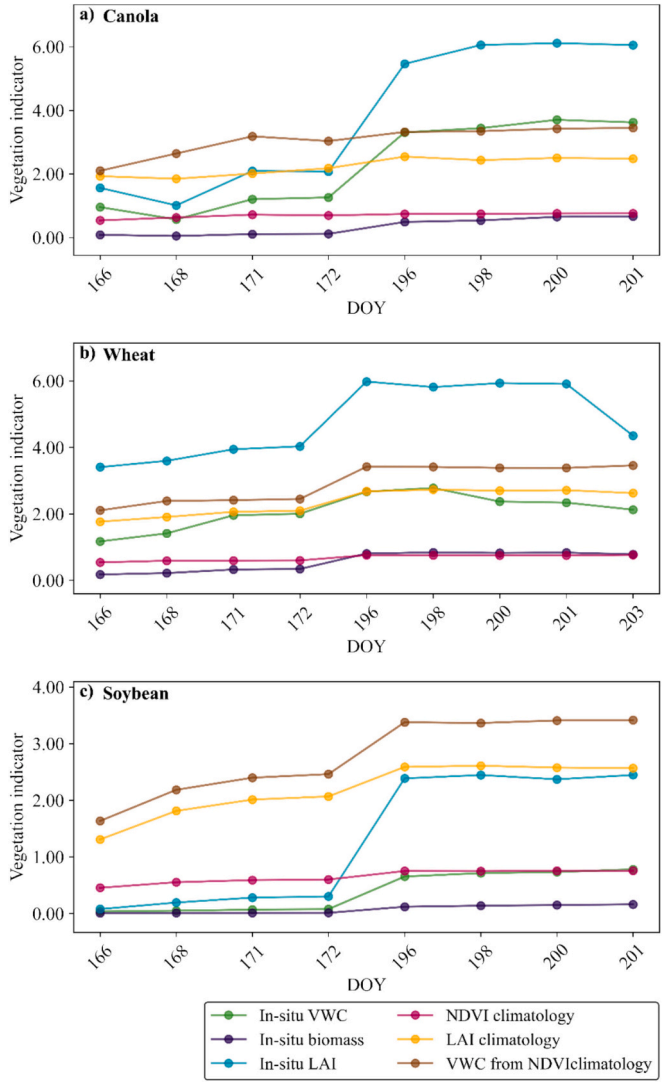

Fig. 8. Trends of in-situ measured VWC, biomass and LAI, as well as NDVI climatology, VWC derived from NDVI climatology, and LAI climatology at the field scale during SMAPVEX16-MB.

unchanged during consecutive two or three observations (Konings et al., 2016; Konings et al., 2017).

Additionally, the H_{rp} values in the original MT-DCA and CMCA are closely aligned, at 0.13 and 0.12, respectively (Table 1) (Konings et al., 2017; Ebtehaj and Bras, 2019), which can characterize the surface roughness of fields such as those covered by canola. However, under each of the four H_{rp} parameterizations, the correlations between VOD and VWC/biomass differ between the two algorithms. This difference is primarily due to variations in their strategies, assumptions, or constraints. Our analysis shows that MT-DCA generally yields accurate results, with strong correlations between VOD and VWC/biomass for canola and soybean, demonstrating high sensitivity (Figs. 3–4). For wheat, scattered VOD data points are observed; despite the scattering, their overall correlation with biomass and VWC remains linear. In summary, each of the three algorithms presents potential advantages for the three crops when coupled with the optimal H_{rp} parameterization—the dynamic H_{rp} model (H_{rp}_*Dyn*). Further, introducing reasonable constraints to MT-DCA may enhance VOD retrieval and improve the understanding of prior information in VOD retrieval.

4.2. Evaluation between LAI and NDVI climatology as prior information

Figs. 6–7 show the correlations between VWC/biomass and VOD retrieved from RDCA, C-MT-DCA, and CMCA, using measured LAI as prior information for VOD, based on the dynamic H_{rp} model with in-situ measured LAI input (H_{rp}_*DynMes*). The selection of prior information does not influence the VOD-VWC linear relationship. Similarly, the regression slopes (parameter *b*) for each crop show negligible cross-algorithm differences, remaining within the aforementioned value range (0.05–0.45).

Compared with the results obtained using NDVI in Figs. 3–4, all VOD estimates show strong correlations with VWC/biomass across the three crops ($R > 0.85$), with high sensitivities, highlighting that accurate prior information for VOD input is far more important than H_{rp}. These results underscore the effectiveness of LAI as prior information for VOD, supported by its ability to effectively characterize VWC/biomass (Fig. 8; Fig. S11). This finding is consistent with numerous published studies, such as those in Saleh et al. (2006), Saleh et al. (2007), Jones et al. (2012), Kerr et al. (2012), and O'Neill et al. (2015), which highlight the strong relationship between VOD and LAI/NDVI. Specifically, VOD exhibits a linear correlation with LAI and a non-linear relationship with NDVI (Grant et al., 2016; Wigneron et al., 2017). Theoretically, LAI offers clearer biophysical significance (Cao et al., 2023): it primarily characterizes leaf quantity and directly reflects vegetation growth and photosynthetic capacity, serving as a key indicator for estimating vegetation biomass and assessing canopy structure (Xiao et al., 2016; Fang et al., 2019). In contrast, VWC is a physiological trait that scales with biomass (dependent on both dry matter and water content per unit dry matter), with most plant water stored in stems. Despite these differences, the shared connection of LAI and VWC to biomass drives their correlation at the canopy scale. Given that VOD is closely related to canopy structure, biomass, and VWC, LAI is likely a suitable prior information for VOD.

As anticipated, the VOD retrieval in RDCA and CMCA is more responsive to variations in vegetation indicators (as prior information) but is insensitive to the constant parameter *b* values (Figs. 6–7, S5–S8). Moreover, RDCA has a strong reliance on prior information and lower sensitivity to H_{rp}. When reliable prior knowledge of LAI is available, RDCA is preferred. However, given uncertainties in satellite-derived LAI, all three algorithms should be evaluated.

4.3. Upscaling LAI and H_{rp} to satellite-derived data

Coupling dynamic H_{rp} (retrieved dynamic H_{rp} /dynamic model-derived H_{rp}) with LAI climatology or NDVI climatology as prior knowledge, the correlations between VOD, VWC, and biomass for RDCA, C-MT-DCA, and CMCA are depicted in Figs. 9–10, S9–S10 and Tables S4-S5. The VOD-VWC/biomass linear relationship is maintained even with varied H_{rp} parameterizations or VOD prior information. For the same crop type, the RDCA and CMCA consistently produce higher sensitivity of VOD to VWC than C-MT-DCA. Overall, LAI climatology outperforms NDVI climatology as prior information in improving VOD retrieval across three algorithms, under both the retrieved dynamic H_{rp} (H_{rp}_*DynRet*) and the dynamic model-derived H_{rp} (H_{rp}_*DynSat*). This improvement is attributed to LAI climatology's superior representation of vegetation characteristics, akin to real-time LAI, in capturing the trends of VWC and biomass (Fig. 8). When combined with retrieved dynamic H_{rp}, LAI climatology further enhances VOD retrieval. Specifically, CMCA achieved the best performance ($R > 0.73$) when constrained by LAI climatology with a 50% multiplicative error. In contrast, the other two algorithms did not consistently improve VOD retrieval for all vegetation types when using retrieved dynamic H_{rp} and LAI climatology as prior information. For example, for soybeans, C-MT-DCA and RDCA showed far lower correlations between VOD and VWC/biomass when compared with NDVI climatology as prior information (Figs. 9–10 (g, h)). This suggests that CMCA's retrieval strategy, supported by

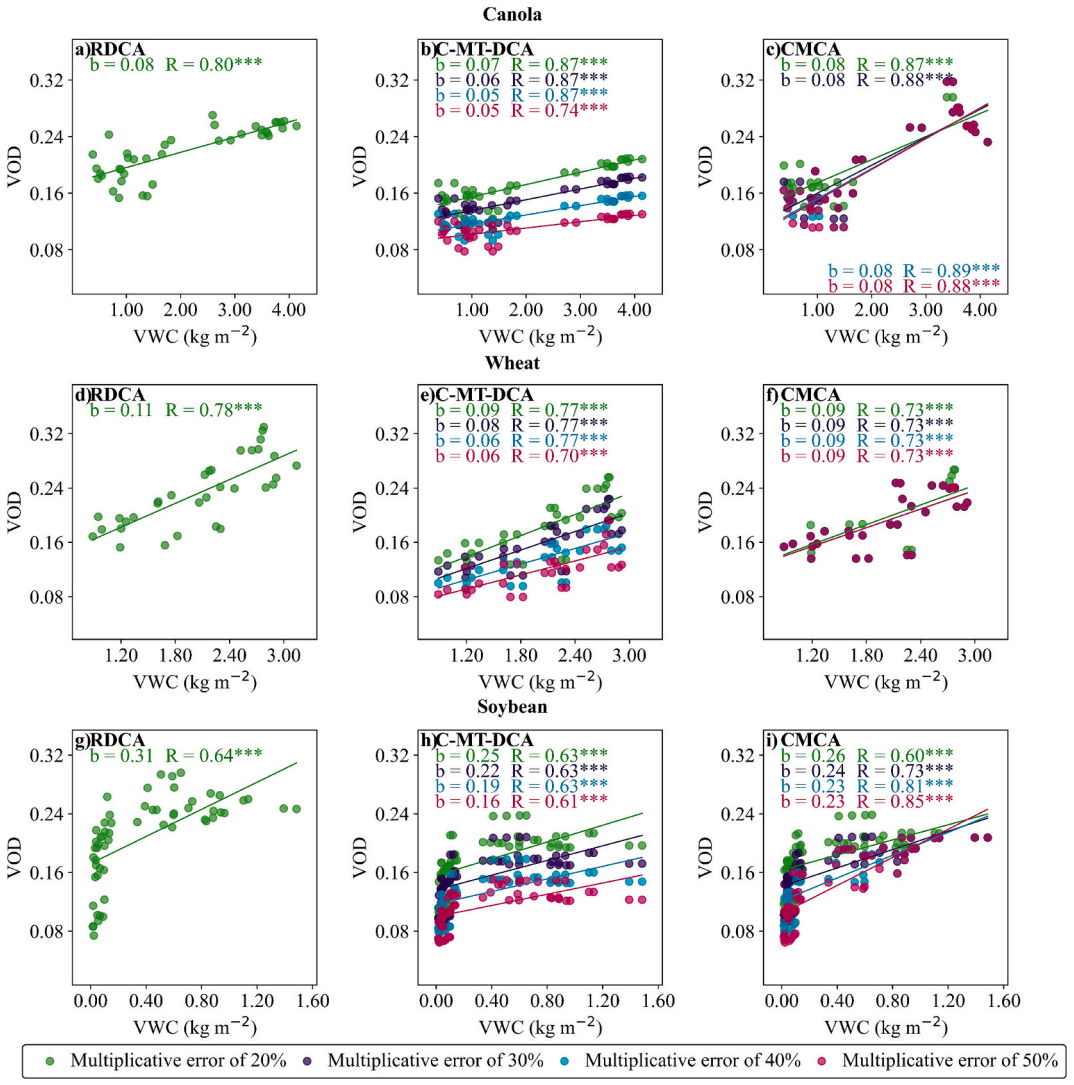

Fig. 9. Correlations between VWC and VOD retrieved from RDCA, MT-DCA with constraint bounds (C-MT-DCA), and CMCA, using H_{rp} retrieved from the τ-ω model via VOD determined by satellite-derived LAI climatology (retrieved dynamic H_{rp}, H_{rp}_*DynRet*), with LAI climatology used as prior information for VOD. Parameter *b* is the slope of the zero-intercept linear regression between VOD and VWC. *** represents statistical significance at the 0.001 significance level ($P < 0.001$).

physical constraints such as a regularization term based on the slow variation of VOD (Ebtehaj and Bras, 2019; O'Neill et al., 2020), provides stability and flexibility, with sensitivity to H_{rp} and prior information of VOD. Specifically, this physical constraint is more theoretically sound than the assumption of C-MT-DCA (Konings et al., 2017; Ebtehaj and Bras, 2019). Compared to RDCA, it helps incorporate more observations, thus increasing the information (Konings et al., 2015). Additionally, it makes CMCA more sensitive to H_{rp} and less reliant on prior information than RDCA (Figs. 3–4, 9–10).

We also observe that this physical constraint generally enables CMCA to retrieve accurate VOD without constraint bounds. However, weak constraints are required when observational noise is high to limit outliers, which explains why CMCA performs well under weak bound constraints. Additionally, combining LAI climatology as prior information with the retrieved dynamic H_{rp} may not introduce additional data or model noise. This reduces errors in VOD retrieval compared with other combinations, including dynamic model-derived H_{rp} with NDVI climatology, dynamic model-derived H_{rp} with LAI climatology, and retrieved dynamic H_{rp} with NDVI climatology (Figs. 9–10 and S9–S10; Tables S4-S5).

The R and RMSE between forward-simulated TB (input with VOD retrievals) and observed TB for the three algorithms confirm that retrieved dynamic H_{rp} (H_{rp}_*DynRet*) combined with LAI climatology is superior (Table S1-S2). Under this combination, all three algorithms achieve high correlation coefficients (R = 0.93–0.97 for horizontal polarization, 0.88–0.97 for vertical polarization) between forward-simulated and observed TB. Among them, CMCA and C-MT-DCA have lower RMSE than RDCA (especially for horizontal polarization); with optimal bound constraints (CMCA: 50% multiplicative error; C-MT-DCA: 40%–50% multiplicative errors), their TB RMSE is further reduced, and CMCA still maintains higher VOD-VWC/biomass correlation (Figs. 9–10). This consistency between numerical accuracy (TB matching) and physical relevance (VOD-vegetation parameter correlation) fully confirms the effectiveness of the improved retrieval strategy.

The sensitivity of the three inversion algorithms to prior information and H_{rp} parameterization is examined by varying one while keeping the other constant, based on the correlation between VOD, VWC, and biomass (referred to as correlation). VOD is retrieved from three algorithms, each providing the best overall performance for the three crops. When using dynamic model-derived H_{rp}, MT-DCA with 40% multiplicative error and CMCA with 40% multiplicative errors achieve the best results. When using retrieved dynamic H_{rp}, MT-DCA with 40% multiplicative error and CMCA with 50% multiplicative errors show optimal performance (Figs. 9–10 and S9–S10). In the following analysis,

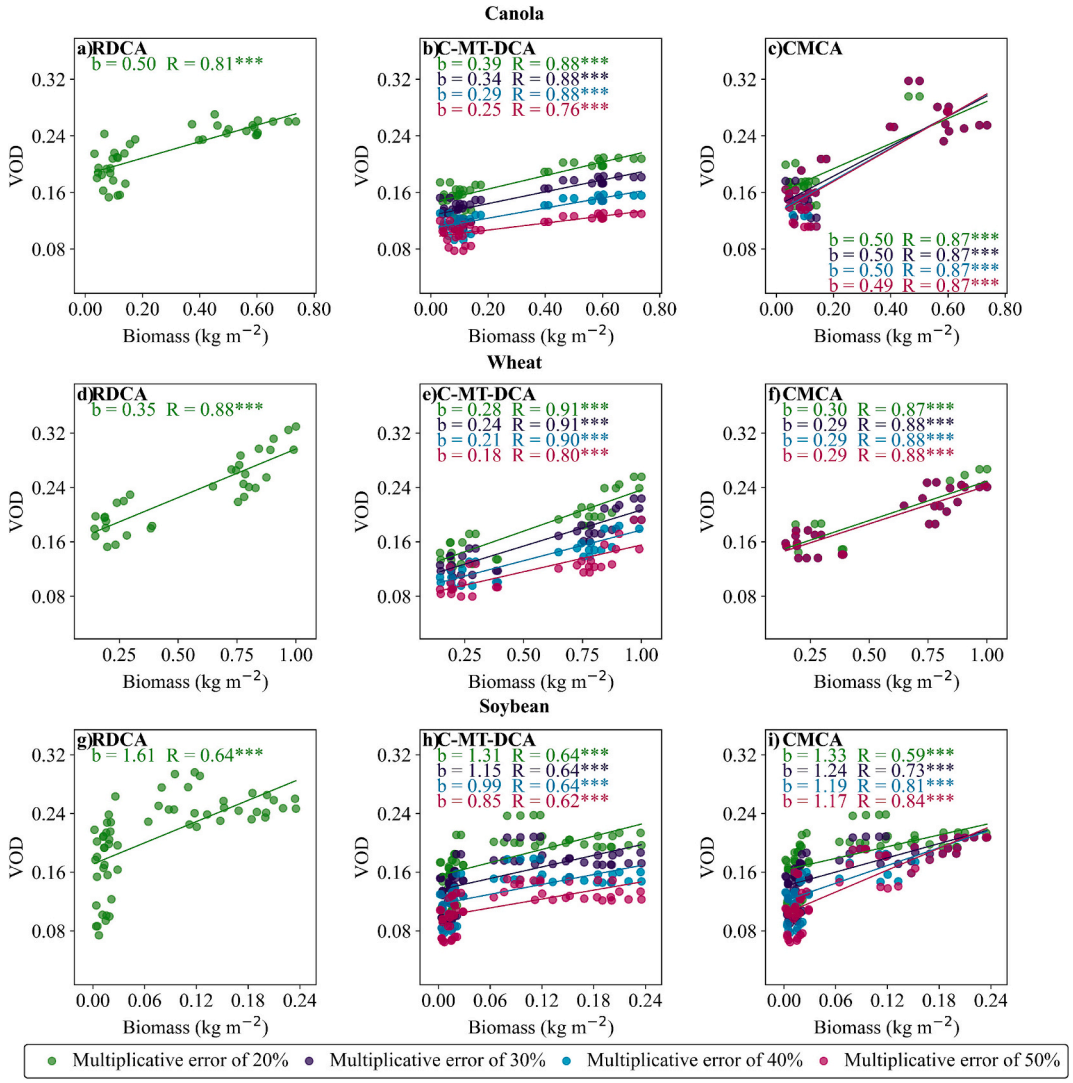

Fig. 10. Correlations between biomass and VOD retrieved from RDCA, MT-DCA with constraint bounds (C-MT-DCA), and CMCA, using H_{rp} retrieved from the τ-ω model via VOD determined by satellite-derived LAI climatology (retrieved dynamic H_{rp}, H_{rp}_*DynRet*), with LAI climatology used as prior information for VOD. Parameter *b* is the slope of the zero-intercept linear regression between VOD and biomass. *** represents statistical significance at the 0.001 significance level ($P < 0.001$).

differences in correlation are categorized as three levels: no difference (< 0.06), higher difference (0.06–0.10), and far higher difference (> 0.10). As discussed in Section 4.1, RDCA is less sensitive to H_{rp}, with similar correlations under both H_{rp} parameterizations (Figs. 9–10 (a, d, g)). On the other hand, RDCA is more sensitive to prior information, as correlation for canola is far higher with LAI climatology than with NDVI climatology (Figs. 9–10 (a)), while soybeans show lower correlations (Figs. 9–10 (g)). In contrast, CMCA is more sensitive to both H_{rp} and prior information. For example, wheat shows large differences in correlation under different H_{rp} parameterizations and prior information constraints (Figs. 9–10 (f)). For soybean, correlation is much higher with LAI climatology than with NDVI climatology (Figs. 9–10 (i)). Additionally, C-MT-DCA is sensitive to prior information and H_{rp} under LAI climatology constraints. For example, under NDVI climatology constraints, C-MT-DCA shows similar correlations across the two H_{rp} parameterizations for all three vegetation types. However, under LAI climatology constraints, the correlation for canola is far higher, compared to NDVI climatology constraint (Figs. 9–10 (b)). With the LAI climatology, canola and wheat show higher correlation with the retrieved dynamic H_{rp} than with the dynamic model-derived H_{rp}, whereas for soybean, the opposite is found (Figs. 9–10). Further analysis indicates that using the retrieved dynamic H_{rp} generally yields higher correlations than the dynamic model-derived H_{rp} for CMCA and C-MT-DCA (Figs. 9–10 (b, c, e, f, h, i)), likely due to the higher uncertainties in the dynamic H_{rp} model and satellite LAI data. This demonstrates that the retrieved dynamic H_{rp} is more effective.

When using the retrieved dynamic H_{rp}, LAI climatology constraints reduce CMCA's sensitivity to multiplicative errors compared to NDVI climatology. For instance, for canola, the correlation between VOD and VWC ranges from $R = 0.38$ to 0.87 under NDVI climatology constraints, but remains steady at $R = 0.87$–0.89 under LAI climatology constraints (Figs. 9–10 (c)). In contrast, C-MT-DCA shows good universality and low sensitivity to multiplicative errors under both climatology constraints (Figs. 9–10 (b, e, h)), further validating the effectiveness of LAI climatology constraints and retrieved dynamic H_{rp}.

4.4. *Validation of the proposed algorithm using independent data*

The development and optimization of the proposed algorithm in this study, including all evaluations of parameterization schemes and prior information (Section 3.2), were conducted exclusively using the SMAPVEX16-MB dataset. To provide an independent evaluation of its

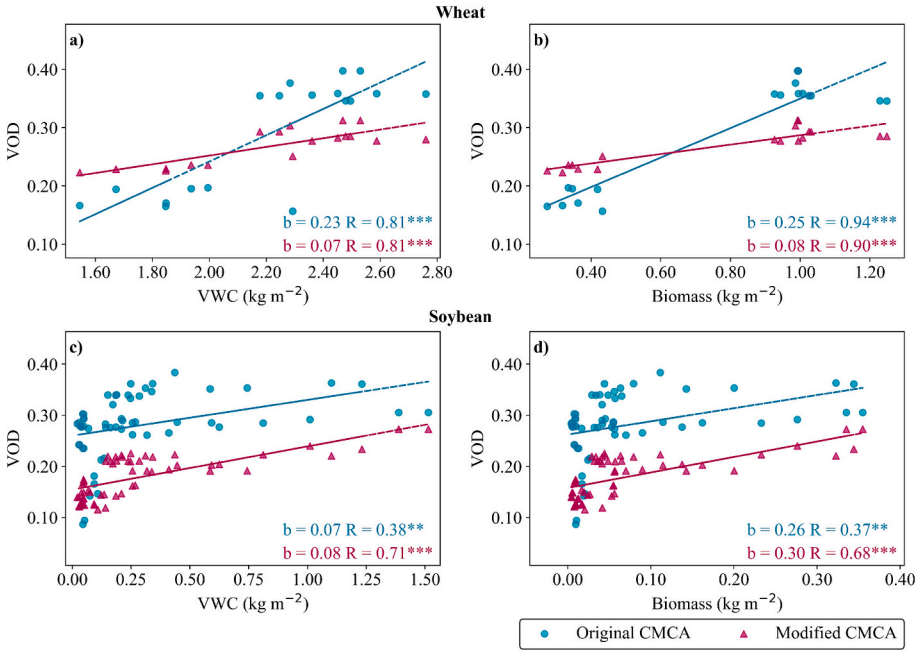

Fig. 11. The validation of the new algorithm with the SMAPVEX12 dataset. Parameter *b* is the slope of the zero-intercept linear regression between VOD and biomass. ** and *** represent statistical significance at the 0.01 and 0.001 significance levels (i.e., $P < 0.01$ and $P < 0.001$), respectively.

Table 3
Relative sensitivity coefficient (S), Pearson correlation coefficient (R), and Root mean square error (RMSE) for retrieved VOD before and after the stochastic perturbation experiment of input parameters including soil temperature (T_s), soil moisture (SM), and leaf area index (LAI).

Perturbation stage	Perturbed parameter	Metrics	Canola	Wheat	Soybean	Total
Before perturbation	/	R	0.88/0.87	0.73/0.88	0.85/0.84	/
After perturbation	T_s	S	3.79	4.59	5.86	4.93
		R	0.90/0.90	0.76/0.84	0.85/0.83	/
		RMSE	0.04	0.06	0.06	0.05
	SM	S	10.88	16.31	8.79	11.00
		R	0.90/0.89	0.77/0.85	0.85/0.84	/
		RMSE	0.05	0.06	0.06	0.06
	LAI	S	11.91	17.02	8.75	11.46
		R	0.88/0.88	0.75/0.83	0.84/0.82	/
		RMSE	0.06	0.07	0.05	0.06

performance, we validated the final selected algorithm configuration (CMCA incorporating LAI climatology and its dynamic H_{rp}) using the SMAPVEX12 dataset. This independent test was designed to validate the algorithm's effectiveness and robustness under different spatiotemporal conditions.

The evaluation with the SMAPVEX12 dataset includes only wheat and soybean, while canola data are unavailable. Overall, our modified retrieval algorithm outperforms the original one (Fig. 11, Table S3). For wheat, the modified algorithm yields VOD values that show significantly less deviation from the best fitted line for VWC/biomass, although the correlation coefficients are similar to the original model. For soybean, the retrieved VOD using the modified model presents a significantly higher correlation with the VWC/biomass compared with the original algorithm. For low-height vegetation such as soybean, where TB has strong soil contributions, optimizing the dynamic H_{rp} appears to contribute more to improving the retrieval performance than for high vegetation like wheat. Additionally, compared with the original algorithm, R between simulated and observed TB has significantly increased, while RMSE has significantly decreased.

4.5. Impact of key parameter uncertainties on VOD retrievals

We analyzed the impact of uncertainties in input parameters (T_s, SM, and LAI) on the uncertainty of VOD retrieval—using an improved algorithm that incorporates LAI climatology and its dynamic H_{rp} into the CMCA—by combining a stochastic perturbation experiment with the τ-ω model (Table 3). Results indicate that although SM and LAI exhibited higher unit perturbation response intensities on VOD retrieval than T_s, the three parameters had comparable impacts under the current perturbation magnitude. This is evidenced by the low RMSE between VOD retrievals in perturbed and unperturbed scenarios. Critically, stochastic perturbations of input parameters only caused a slight offset in retrieved VOD values; they did not influence the physical causal relationship between VOD and VWC/biomass, nor did they affect VOD's temporal trends. This preserved VOD's robust ability to characterize VWC/biomass while verifying the stability of the τ-ω model and the reliability of VOD estimation.

While the above results quantify the impact of parameter perturbations on VOD retrieval, more importantly, random parameter perturbations only alter the numerical value of retrieved VOD and do not undermine this physical causal relationship. This stability stems from the core physical meaning of VOD: it essentially represents the vegetation's microwave attenuation capacity, which is determined by VWC, biomass and structure (Ulaby and Jedlicka, 1984; Jackson and Schmugge, 1991; Chahuan et al., 1994; Kurum, 2013; Long and Ulaby, 2015; Gao et al., 2020a). Uncertainties in input parameters do not alter the relational logic of "vegetation properties → microwave attenuation → VOD". Additionally, perturbations are non-directional fluctuations

within a reasonable physical range, which only cause a slight overall offset in retrieved VOD values without disrupting its temporal trends (e.g., the low→high→low pattern of VOD during the growing season). Ultimately, this maintains VOD's stable capability to characterize VWC and biomass.

5. Conclusion

Although Normalized Difference Vegetation Index (NDVI) climatology and a fixed surface roughness are employed to constrain various retrieval algorithms for SMAP soil moisture (SM) and vegetation optical depth (VOD), NDVI is prone to saturation, and a constant surface roughness does not account for the variations driven by agricultural activities. This results in inaccuracies in SM and VOD retrieval. To address this, this study proposes an alternative algorithm for VOD retrieval using the SMAPVEX2016-MB dataset. This algorithm builds on the retrieval strategy of CMCA, incorporating satellite-derived LAI climatology as prior information for VOD and a flexible surface roughness parameterization, with the key output being enhanced VOD retrieval through optimizing surface roughness (H_{rp}) parameterization and VOD prior information. The algorithm's performance is assessed by comparing its VOD retrievals with in-situ VWC and biomass from the SMAPVEX2012 dataset.

The τ-ω model performs best with in-situ measured LAI as prior information across the three retrieval algorithms (RDCA, MT-DCA with constrained values, and CMCA), mainly because LAI is not prone to saturation and effectively characterizes vegetation structure changes. Additionally, the evaluation of four parameterization schemes—two models based on geometric characteristics with constant values, one dynamic model based on microwave observation and vegetation information with dynamic values, and the values used in the original algorithm—reveals that dynamic parameterization provides the most accurate VOD retrieval. Consequently, incorporating dynamic surface roughness into the retrieval algorithm enhances SMAP VOD retrieval, in addition to prior information of VOD. Notably, when prior information sufficiently describes vegetation changes, it is far more important than surface roughness. Due to uncertainties in the satellite-derived LAI data, the dynamic model, and their interaction during VOD retrieval, directly calculating dynamic surface roughness using satellite-derived LAI in the dynamic model is less effective than using in-situ LAI. When satellite-derived LAI climatology is used as prior information in the three retrieval algorithms, CMCA performs better with the derived dynamic surface roughness via VOD determined by LAI climatology compared with NDVI climatology. This discrepancy is mainly due to differences in retrieval strategies and uncertainties in satellite-derived data.

Theoretically, using LAI to constrain VOD is more effective for diverse vegetation types, as LAI is less prone to saturation and more accurately reflects vegetation changes across different ecosystems. Future research should focus on the effects of real-time LAI, as it can better capture vegetation responses to climate extremes. Additionally, the impact of different surface roughness parameterizations (e.g., monthly, seasonally or annual averages, or constant surface roughness) needs to be explored. From this perspective, we plan to investigate these effects on a large scale in SMAP pixels.

Finally, the VOD retrieved from RDCA, MT-DCA, and CMCA can characterize VWC and biomass along with crop growth. Among these methods, RDCA and CMCA demonstrate broad applicability across all three crops. In contrast, MT-DCA performs better on some crop types (canola and soybean) but worse on others (wheat).

CRediT authorship contribution statement

Hui Zhang: Writing – review & editing, Writing – original draft, Visualization, Validation, Software, Methodology, Formal analysis, Conceptualization. **Zhou Shi:** Writing – review & editing, Validation, Supervision, Funding aquisition. **Lun Gao:** Writing – review & editing, Methodology. **Zhibin Sun:** Methodology. **Bing He:** Methodology. **Yixiang Wang:** Writing – review & editing. **Hongquan Wang:** Writing – review & editing, Visualization, Methodology, Investigation.

Declaration of competing interest

The authors declare that they have no known competing financial interests or personal relationships that could have appeared to influence the work reported in this paper.

Acknowledgments

The study was funded by National Natural Science Foundation of China (W2412107 & 32171781) and the Fundamental and Interdisciplinary Disciplines Breakthrough Plan of the Ministry of Education of China (JYB2025XDXM909). Lun Gao was supported by the World Resources Institute (WRI) grant (G3275) and U.S. Geological Survey (USGS) grant (G24AC00247-00). The authors express gratitude to the National Aeronautics and Space Administration (NASA) for collecting the PALS datasets. The authors also extend appreciation to all the crews of SMAPVEX16-MB field campaigns for their efforts in collecting these comprehensive datasets, and to the anonymous reviewers for their valuable feedback in improving the paper. A portion of this work was supported by contributions from the Jet Propulsion Laboratory, California Institute of Technology, under a contract with NASA.

Appendix A. Supplementary data

Supplementary data to this article can be found online at https://doi.org/10.1016/j.rse.2026.115443.

Data availability

Data will be made available on request.

References

Abban, B.K., Papanicolaou, A.N., Giannopoulos, C.P., Dermisis, D.C., Wacha, K.M., Wilson, C.G., Elhakeem, M., 2017. Quantifying the changes of soil surface microroughness due to rainfall impact on a smooth surface. Nonlinear Process. Geophys. 24 (3), 569–579.

Abbott, B.W., Bishop, K., Zarnetske, J.P., Minaudo, C., Chapin, F.S., Krause, S., Plont, S., 2019. Human domination of the global water cycle absent from depictions and perceptions. Nat. Geosci. 12 (7), 533–540.

Adagbasa, E.G., Adelabu, S.A., Okello, T.W., 2019. Application of deep learning with stratified k-fold for vegetation species discrimation in a protected mountainous region using sentinel-2 image. Geocarto Int. 37 (1), 142–162.

Adams, R.A., Fournier, J.J.F., 2003. Sobolev Spaces, p. 140.

Al Bitar, A., Mialon, A., Kerr, Y.H., Cabot, F., Richaume, P., Jacquette, E., Quesney, A., Mahmoodi, A., Tarot, S., Parrens, A., 2017. The global SMOS level 3 daily soil moisture and brightness temperature maps. Earth Syst. Sci. Data 9 (1), 293–315.

Basharinov, A., Shutko, A., 1975. Simulation studies of the SHF radiation characteristics of soils under moist conditions. In: NASA Tech. Transl. TT F-16, 1975.

Baur, M.J., Jagdhuber, T., Feldman, A.F., Akbar, R., Entekhabi, D., 2019. Estimation of relative canopy absorption and scattering at l-, C-and X-bands. Remote Sens. Environ. 233, 111384.

Bhuiyan, H.A.K.M., McNairn, H., Powers, J., Friesen, M., Pacheco, A., Jackson, T.J., Cosh, M.H., Colliander, A., Berg, A., Rowlandson, T., Bullock, P., Magagi, R., 2018. Assessing SMAP soil moisture scaling and retrieval in the Carman (Canada) study site. Vadose Zone J. 17, 180132.

Bindlish, R., Jackson, T., Sun, R., Cosh, M., Yueh, S., Dinardo, S., 2009. Combinedpassive and active microwave observations of soil moisture during CLASIC. IEEE Geosci. Remote Sens. Lett. 6 (4), 644–648.

Bindlish, R., Jackson, T., Zhao, T., 2011. A MODIS-based vegetation index climatology. In: Remote Sensing and Modeling of Ecosystems for Sustainability VIII, 8156, pp. 41–48.

Bindlish, R., Jackson, T., Cosh, M., Zhao, T.J., O'Neill, P., 2015. Global soil moisture from the Aquarius/SAC-D satellite: description and initial assessment. IEEE Geosci. Remote Sens. Lett. 12 (5), 923–927.

Brandt, M., Wigneron, J.P., Chave, J., Tagesson, T., Penuelas, J., Ciais, P., Rasmussen, K., Tian, F., Mbow, C., Al-Yaari, A., Rodríguez-Fernández, N., Schurgers, G., Zhang, W. M., Chang, J.F., Kerr, Y., Verger, A., Tucker, C., Mialon, A., Rasmussen, L.V., Fan, L., Fensholt, R., 2018. Satellite passive microwaves reveal recent climate-induced carbon losses in African drylands. Nat. Ecol. Evol. 2, 827–835.

Byrd, R.H., Schnabel, R.B., Shultz, G.A., 1987. A trust region algorithm for nonlinearly constrained optimization. SIAM J. Numer. Anal. 24 (5), 1152–1170.
Cao, S., Li, M., Zhu, Z., Wang, Z., Zha, J., Zhao, W., Duanmu, Z., Chen, J., Zheng, Y., Chen, Y., Myneni, R.B., Piao, S., 2023. Spatiotemporally consistent global dataset of the GIMMS leaf area index (GIMMS LAI4g) from 1982 to 2020. Earth Syst. Sci. Data. 15, 4877–4899.
Celis, M.R., Dennis, J.E., Tapia, R.A., 1984. A trust region strategy for nonlinear equality constrained optimization. In: Boggs, P.T., Byrd, R.H., Schnabel, R.B. (Eds.), Numerical Optimization 1984. SIAM, Philadelphia, pp. 71–82, 1985.
Chahuan, N.S., Le Vine, D.M., Lang, R.H., 1994. Discrete scattering model for microwave radar and radiometer response to corn: comparison of theory and data. IEEE Trans. Geosci. Remote Sens. 32 (2), 416–426.
Chan, S., Hunt, R., Bindlish, R., Njoku, E., Kimball, J., Jackson, T., 2013. Ancillary data report for vegetation water content. In: SMAP Project Document.
Chaubell, M.J., Yueh, S.H., Dunbar, R.S., Colliander, A., Chen, F., Chan, S.K., Entekhabi, D., Bindlish, R., O'Neill, P.E., Asanuma, J., Berg, A.A., Bosch, D.D., Caldwell, T., Cosh, M.H., Collins, C.H., Martínez-Fernández, J., Seyfried, M., Starks, P.J., Su, Z.B., Thibeault, M., Walker, J., 2020. Improved SMAP dual-channel algorithm for the retrieval of soil moisture. IEEE Trans. Geosci. Remote Sens. 58 (6), 3894–3905.
Chaubell, J., Yueh, S., Dunbar, R.S., Colliander, A., Entekhabi, D., Chan, S.K., Chen, F., Xu, X., Bindlish, R., O'Neill, P., Asanuma, J., 2021. Regularized dual-channel algorithm for the retrieval of soil moisture and vegetation optical depth from SMAP measurements. IEEE J. Sel. Top. Appl. Earth Obs. Remote Sens. 15, 102–114.
Choudhury, B.J., Schmugge, T.J., Chang, A., Newton, R.W., 1979. Effect of surface-roughness on the microwave emission from soils. J. Geophys. Res. 84 (C9), 5699–5706.
Choudhury, B., Schmugge, T., Mo, T., 1982. A parameterization of effective soil temperature for microwave emission. J. Geophys. Res. 87, 1301–1304.
Colliander, A., Chan, S., Kim, S.B., Das, N., Yueh, S., Cosh, M., Bindlish, A., Jackson, T., Njoku, E., 2012. Long term analysis of PALS soil moisture campaign measurements for global soil moisture algorithm development. Remote Sens. Environ. 121, 309–322.
Colliander, A., Jackson, T., McNairn, H., Chazanoff, S., Dinardo, S., Latham, B., O'Dwyer, I., Chun, W., Yueh, S., Njoku, E., 2015. Comparison of airborne passive and active L-band system (PALS) brightness temperature measurements to SMOS observations during the SMAP validation experiment 2012 (SMAPVEX12). IEEE Geosci. Remote Sens. Lett. 12 (4), 801–805.
Colliander, A., Njoku, E.G., Jackson, T.J., Chazanoff, S., McNairn, H., Powers, J., Cosh, M.H., 2016. Retrieving soil moisture for non-forested areas using PALS radiometer measurements in SMAPVEX12 field campaign. Remote Sens. Environ. 184, 86–100.
Colliander, A., Cosh, M.H., Misra, S., Jackson, T.J., Crow, W.T., Powers, J., McNairn, H., Bullock, P., Berg, A., Magagi, R., Gao, Y., Bindlish, R., Williamson, R., Ramos, I., Latham, B., O'Neill, P., Yueh, S., 2019. Comparison of high-resolution airborne soil moisture retrievals to SMAP soil moisture during the SMAP validation experiment 2016 (SMAPVEX16). Remote Sens. Environ. 227, 137–150.
Cosh, M.H., White, W.A., Colliander, A., Jackson, T.J., Prueger, J.H., Hornbuckle, B.K., Hunt, E.R., McNairn, H., Powers, J., Walker, V.A., Bullock, P., 2019. Estimating vegetation water content during the soil moisture active passive validation experiment 2016. J. Appl. Remote. Sens. 13, 014516.
Dannenberg, M., Wang, X., Yan, D., Smith, W., 2020. Phenological characteristics of global ecosystems based on optical, fluorescence, and microwave remote sensing. Remote Sens. 12 (4), 671.
de Jeu, R.A.M., Holmes, T.R.H., Panciera, R., Walker, J.P., 2009. Parameterization of the land parameter retrieval model for L-band observations using the NAFE'05 data set. IEEE Geosci. Remote Sens. Lett. 6 (04), 630–634.
Du, J., Jones, L., Kimball, J., 2017. Daily Global Land Parameters Derived from AMSR-E and AMSR2 (Version 2.0). National Snow Ice Data Center, Boulder, CO, USA.
Ebtehaj, A., Bras, R.L., 2019. A physically constrained inversion for high resolution passive microwave retrieval of soil moisture and vegetation water content in L-band. Remote Sens. Environ. 233, 111346.
Entekhabi, D., Njoku, E.G., O'Neill, P.E., Kellogg, K.H., Crow, W.T., Edelstein, W.N., Entin, J.K., Goodman, S.D., Jackson, T.J., Johnson, J., Kimball, J., Piepmeier, J.R., Koster, R.D., Martin, N., McDonald, K.C., Moghaddam, M., Moran, S., Reichle, R., Shi, J.C., Spencer, M.W., Thurman, S.W., Tsang, L., Van Zyl, J., 2010. The soil moisture active passive (SMAP) mission. Proc. IEEE 98 (5), 704–716.
Escorihuela, M.J., Kerr, Y.H., de Rosnay, P., Wigneron, J.P., Calvet, J.C., Lemaître, F., 2007. A simple model of the bare soil microwave emission at L-band. IEEE Trans. Geosci. Remote Sens. 45 (7), 1978–1987.
Fagerlund, E., Kleman, B., Sellin, L., Svensson, H., 1970. Physical studies of nature by thermal mapping. Earth Sci. Rev. 6 (3), 169–180.
Fan, L., Wigneron, J.P., Ciais, P., Chave, J., Brandt, M., Fensholt, R., Saatchi, S.S., Bastos, A., Al-Yaari, A., Hufkens, K., Qin, Y.W., Xiao, X.M., Chen, C., Myneni, R.B., Fernandez-Moran, R., Mialon, A., Rodríguez-Fernández, N.J., Kerr, Y., Tian, F., Peñuelas, J., 2019. Satellite observed pantropical carbon dynamics. Nat. Plants 5 (9), 944–951.
Fan, L., Cui, T.X., Wigneron, J.P., Ciais, P., Sitch, S., Brandt, M., Li, X., Niu, S.L., Xiao, X. M., Chave, J., Wu, C.Y., Li, W., Yuan, W.P., Xing, Z.P., Li, X.J., Wang, M.J., Liu, X.Z., Chen, X.Z., Qin, Y.W., Yang, H., Tang, Q., Li, Y.C., Ma, M.G., Fensholt, R., 2024. Dominant role of the non-forest woody vegetation in the post 2015/16 El Niño tropical carbon recovery. Glob. Chang. Biol. 30 (7), e17423.
Fang, H., Baret, F., Plummer, S., Schaepman-Strub, G., 2019. An overview of global leaf area index (LAI): methods, products, validation, and applications. Rev. Geophys. 57 (3), 739–799.
Feldman, A.F., Short Gianotti, D.J., Konings, A.G., McColl, K.A., Akbar, R., Salvucci, G. D., Entekhabi, D., 2018. Moisture pulse-reserve in the soil-plant continuum observed across biomes. Nat. Plants 4 (12), 1026–1033.
Feng, S.J., Gao, L., Qiu, J.X., Liu, X.P., Crow, W.T., Zhao, T.J., Tan, C., Wang, S.H., Wigneron, J.P., 2025. Can real-time NDVI observations better constrain SMAP soil moisture retrievals? Remote Sens. Environ. 318, 114569.
Gao, L., Sadeghi, M., Ebtehaj, A., Wigneron, J.P., 2020a. A temporal polarization ratio algorithm for calibration-free retrieval of soil moisture at L-band. Remote Sens. Environ. 249, 112019.
Gao, L., Sadeghi, M., Feldman, A.F., Ebtehaj, A., 2020b. A spatially constrained multichannel algorithm for inversion of a first-order microwave emission model at L-band. IEEE Trans. Geosci. Remote Sens. 58 (11), 8134–8146.
Gao, L., Sadeghi, M., Ebtehaj, A., 2020c. Microwave retrievals of soil moisture and vegetation optical depth with improved resolution using a combined constrained inversion algorithm: application for SMAP satellite. Remote Sens. Environ. 239 (15), 111662.
Gao, L., Ebtehaj, A., Chaubell, M.J., Sadeghi, M., Li, X., Wigneron, J.P., 2021. Reappraisal of SMAP inversion algorithms for soil moisture and vegetation optical depth. Remote Sens. Environ. 264, 112627.
Ghorbanzadeh, O., Shahabi, H., Mirchooli, F., Valizadeh Kamran, K., Lim, S., Aryal, J., Jarihani, B., Blaschke, T., 2020. Gully erosion susceptibility mapping (GESM) using machine learning methods optimized by the multi-collinearity analysis and K-fold cross-validation. Geomat. Nat. Hazards Risk. 11, 1653–1678.
Grant, J.P., Wigneron, J.P., de Jeu, R.A.M., Lawrence, H., Mialon, A., Richaume, P., Al Bitar, A., Drusch, M., van Marle, M.J.E., Kerr, Y., 2016. Comparison of SMOS and AMSR-E vegetation optical depth to four MODIS-based vegetation indices. Remote Sens. Environ. 172, 87–100.
Hamilton, S.E., Friess, D.A., 2018. Global carbon stocks and potential emissions due to mangrove deforestation from 2000 to 2012. Nat. Clim. Chang. 8 (3), 240–244.
Jackson, T.J., 1993. Measuring surface soil moisture using passive microwave remote sensing. Hydrol. Process. 7, 139–152.
Jackson, T.J., Schmugge, T.J., 1991. Vegetation effects on the microwave emission of soils. Remote Sens. Environ. 36 (3), 203–212.
Jiang, Z., Huete, A.R., Didan, K., Miura, T., 2008. Development of a two-band enhanced vegetation index without a blue band. Remote Sens. Environ. 112, 3833–3845.
Jones, M.O., Kimball, J.S., Jones, L.A., McDonald, K.C., 2012. Satellite passive microwave detection of North America start of season. Remote Sens. Environ. 123, 324–333.
Jones, M.O., Kimball, J.S., Small, E.E., Larson, K.M., 2014. Comparing land surface phenology derived from satellite and GPS network microwave remote sensing. Int. J. Biometeorol. 58 (6), 1305–1315.
Karthikeyan, L., Pan, M., Konings, A.G., Piles, M., Fernandez-Moran, R., Kumar, D.N., Wood, E.F., 2019. Simultaneous retrieval of global scale Vegetation Optical Depth, surface roughness, and soil moisture using X-band AMSR-E observations. Remote Sens. Environ. 234, 111473.
Kerr, Y.H., Waldteufel, P., Wigneron, J.P., Delwart, S., Cabot, F., Boutin, J., Escorihuela, M.J., Font, J., Reul, N., Gruhier, C., Juglea, S.E., Drinkwater, M.R., Hahne, A., Martín-Neira, M., Mecklenburg, S., 2010. The SMOS mission: new tool for monitoring key elements of the global water cycle. Proc. IEEE 98 (5), 666–687.
Kerr, Y.H., Waldteufel, P., Richaume, P., Wigneron, J.P., Ferrazzoli, P., Mahmoodi, A., Leroux, D., 2012. The SMOS soil moisture retrieval algorithm. IEEE Trans. Geosci. Remote Sens. 50 (5), 1384–1403.
Konings, A.G., McColl, K.A., Piles, M., Entekhabi, D., 2015. How many parameters can be maximally estimated from a set of measurements? IEEE Geosci. Remote Sens. Lett. 12 (5), 1081–1085.
Konings, A.G., Piles, M., Rötzer, K., McColl, K.A., Chan, S.K., Entekhabi, D., 2016. Vegetation optical depth and scattering albedo retrieval using time series of dual-polarized L-band radiometer observations. Remote Sens. Environ. 172, 178–189.
Konings, A.G., Piles, M., Das, N., Entekhabi, D., 2017. L-band vegetation optical depth and effective scattering albedo estimation from SMAP. Remote Sens. Environ. 198, 460–470.
Konkathi, P., Karthikeyan, L., 2022. Error and uncertainty characterization of soil moisture and VOD retrievals obtained from L-band SMAP radiometer. Remote Sens. Environ. 280, 113146.
Kumar, S.V., Holmes, T.R., Bindlish, R., de Jeu, R., Peters-Lidard, C., 2020. Assimilation of vegetation optical depth retrievals from passive microwave radiometry. Hydrol. Earth Syst. Sci. 24 (7), 3431–3450.
Kurum, M., 2013. Quantifying scattering albedo in microwave emission of vegetated terrain. Remote Sens. Environ. 129, 66–74.
Laurin, G.V., Vittucci, C., Tramontana, G., Ferrazzoli, P., Guerriero, L., Papale, D., 2020. Monitoring tropical forests under a functional perspective with satellite-based vegetation optical depth. Glob. Chang. Biol. 26 (6), 3402–3416.
Lawrence, H., Wigneron, J.P., Demontoux, F., Mialon, A., Kerr, Y.H., 2013. Evaluating the semiempirical H-Q model used to calculate the L-band emissivity of a rough bare soil. IEEE Trans. Geosci. Remote Sens. 51 (7), 4075–4084.
Lawrence, H., Wigneron, J.P., Richaume, P., Novello, N., Grant, J., Mialon, A., Al Bitar, A., Merlin, O., Guyon, D., Leroux, D., Bircher, S., Kerr, Y., 2014. Comparison between SMOS vegetation optical depth products and MODIS vegetation indices over crop zones of the USA. Remote Sens. Environ. 140, 396–406.
Li, X., Wigneron, J.P., Frappart, F., Fan, L., Ciais, P., Fensholt, R., Entekhabi, D., Brandt, M., Konings, A.G., Liu, X.Z., Wang, M.J., Al-Yaari, A., Moisy, C., 2021. Global-scale assessment and inter-comparison of recently developed/reprocessed microwave satellite vegetation optical depth products. Remote Sens. Environ. 253, 112208.
Li, X., Wigneron, J.P., Fan, L., Frappart, F., Yueh, S.H., Colliander, A., Ebtehaj, A., Gao, L., Fernandez-Moran, R., Liu, X., Wang, M., 2022. A new SMAP soil moisture

and vegetation optical depth product (SMAP-IB): algorithm, assessment and inter-comparison. Remote Sens. Environ. 271, 112921.
Liu, Y.Y., van Dijk, A.I.J.M., de Jeu, R.A.M., Canadell, J.G., McCabe, M.F., Evans, J.P., Wang, G.J., 2015. Recent reversal in loss of global terrestrial biomass. Nat. Clim. Chang. 5, 470–474.
Long, D., Ulaby, F., 2015. Microwave Radar and Radiometric Remote Sensing. Artech.
Martens, B., Lievens, H., Colliander, A., Jackson, T.J., Verhoest, N.E.C., 2015. Estimating effective roughness parameters of the L-MEB model for soil moisture retrieval using passive microwave observations from SMAPVEX12. IEEE Trans. Geosci. Remote Sens. 53 (7), 409–4103.
McNairn, H., Jackson, T., Wiseman, G., Bélair, S., Berg, A., Bullock, P., Colliander, A., Cosh, M.H., Kim, S.B., Magagi, R., Moghaddam, M., Njoku, E.G., Adam, J.R., Homayouni, S., Ojo, E.R.T., Rowlandson, T.L., Shang, J.L., Goïta, K., Hosseini, M., 2015. The soil moisture active passive validation experiment 2012 (SMAPVEX12): prelaunch calibration and validation of the SMAP soil moisture algorithms. IEEE Trans. Geosc. Remote Sens. 53 (5), 2784–2801.
McNairn, H., Jackson, T.J., Powers, J., Bélair, S., Berg, A., Bullock, P., Colliander, A., Cosh, M.H., Kim, S.B., Magagi, R., Pacheco, A., Merzouki, A., 2016. SMAP Validation Experiment 2016 in Manitoba (SMAPVEX16-MB), Canada, Experiment Plan. Agriculture and Agri-Food Canada.
McNairn, H., Jackson, T.J., Powers, J., Bélair, S., Berg, A., Bullock, P., Colliander, A., Cosh, M.H., Kim, S.B., Magagi, R., Pacheco, A., Merzouki, A., 2017. SMAPVEX16 Database Report. Agriculture and Agri-Food Canada.
Mialon, A., Wigneron, J.P., de Rosnay, P., Escorihuela, M.J., Kerr, Y.H., 2012. Evaluating the L-MEB model from long-term microwave measurements over a rough field, SMOSREX 2006. IEEE Trans. Geosci. Remote Sens. 50 (5), 1458–1467.
Mironov, V.L., Kosolapova, L.G., Fomin, S.V., 2009. Physically and mineralogically based spectroscopic dielectric model for moist soils. IEEE Trans. Geosci. Remote Sens. 47 (7), 2059–2070.
Mironov, V.L., Kosolapova, L.G., Lukin, Y.I., Karavaysky, A.Y., Molostov, I.P., 2017. Temperature-and texture-dependent dielectric model for frozen and thawed mineral soils at a frequency of 1.4 GHz. Remote Sens. Environ. 200, 240–249.
Mo, T., Choudhury, B.J., Schmugge, T.J., Wang, J.R., Jackson, T.J., 1982. A model for microwave emission from vegetation-covered fields. J. Geophys. Res. Oceans. 87 (C13), 11229–11237.
Momen, M., Wood, J.D., Novick, K.A., Pangle, R., Pockman, W.T., McDowell, N.G., Konings, A.G., 2017. Interacting effects of leaf water potential and biomass on vegetation optical depth. J. Geophys. Res-Biogeo. 122 (11), 3031–3046.
Montpetit, B., Royer, A., Wigneron, J.P., Chanzy, A., Mialon, A., 2015. Evaluation of multi-frequency bare soil microwave reflectivity models. Remote Sens. Environ. 162, 186–195.
Narayan, U., Lakshmi, V., Njoku, E.G., 2004. Retrieval of soil moisture from Passive and Active L/S Band Sensor (PALS) observations during the soil moistureexperiment in 2002 (SMEX02). Remote Sens. Environ. 92, 483–496.
Njoku, E.G., Entekhabi, D., 1996. Passive microwave remote sensing of soil moisture. J. Hydrol. 184, 101–129.
Njoku, E.G., Wilson, W.J., Yueh, S.H., Dinardo, S.J., Li, F.K., Jackson, T.J., Lakshmi, V., Bolten, J., 2002. Observations of soil moisture using a passive and active low frequency microwave airborne sensor during SGP99. IEEE Trans. Geosci. Remote Sens. 40 (12), 2659–2673.
Njoku, E.G., Jackson, T.J., Lakshmi, V., Chan, T.K., Nghiem, S.V., 2003. Soil moisture retrieval from AMSR-E. IEEE Trans. Geosci. Remote Sens. 41 (2), 215–229.
O'Neill, P., Chan, S., Njoku, E., Jackson, T., Bindlish, R., 2015. Soil Moisture Active Passive (SMAP) Algorithm Theoretical Basis Document Level 2 & 3 Soil Moisture (Passive) Data Products. Jet Propulsion Laboratory, NASA, Pasadena, CA, USA.
O'Neill, P., Bindlish, R., Chan, S., Chaubell, J., Colliander, A., Njoku, E., Jackson, T., 2020. Algorithm Theoretical Basis Document Level 2 & 3 Soil Moisture (Passive) Data Products (No. JPL D-66480). Jet Propulsion Laboratory, California Institute of Technology, Pasadena, CA.
Owe, M., de Jeu, R., Walker, J., 2001. A methodology for surface soil moisture and vegetation optical depth retrieval using the microwave polarization difference index. IEEE Trans. Geosc. Remote Sens. 39 (8), 1643–1654.
Owe, M., de Jeu, R., Holmes, T., 2008. Multisensor historical climatology of satellitederived global land surface moisture. J. Geophys. Res. Earth Surf. 113.
Pan, M., Sahoo, A.K., Wood, E.F., 2014. Improving soil moisture retrievals from a physically-based radiative transfer model. Remote Sens. Environ. 140, 130–140.
Panciera, R., Walk, J.P., Merlin, O., 2009. Improved understanding of soil surface roughness parameterization for L-band passive microwave soil moisture retrieval. IEEE Geosci. Remote Sens. Lett. 6 (04), 625–629.
Pardé, M., Wigneron, J.P., Chanzy, A., Waldteufel, P., Kerr, Y., Huet, S., 2003. Retrieving surface soil moisture over a wheat field: comparison of different methods. Remote Sens. Environ. 87 (2–3), 334–344.
Parrens, M., Wigneron, J.P., Richaume, P., Mialon, A., Al Bitar, A., Fernandez-Moran, R., Al-Yaari, A., Kerr, Y.H., 2016. Global-scale surface roughness effects at L-band as estimated from SMOS observations. Remote Sens. Environ. 181, 122–136.
Peischl, S., Walker, J.P., Ryu, D., Kerr, Y.H., Panciera, R., Rudiger, C., 2012. Wheat canopy structure and surface roughness effects on multiangle observations at L-band. IEEE Trans. Geosci. Remote Sens. 50, 1498–1506.
Poulter, B., Murray-Tortarolo, G., Hayes, D.J., Ciais, P., Andrew, R.M., Bastos, A., Byrne, B., Butman, D., Canadell, J.G., Chatterjee, A., Domke, G., Feldman, A., Foster, K., Hunka, N., Jackson, R.B., Kurz, W.A., Lindquist, A., Liu, M.D., Luijkx, I., Mialon, A., Michalak, A.M., Miller, J., Obermeier, W.A., Pan, N.Q., Randerson, J.T., Raymond, P.A., Regnier, P., Resplandy, L., Rocher-Ros, G., Rodríguez-Fernández, N., Rosentreter, J., Salazar-Neira, J.C., Tank, S.E., Tian, H.Q., Vargas, R., Villalobos, Y., Wang, J.A., Wei, X.Y., Wickland, K.P., Williams, C., Windham-Myers, L., Woodall, C., Ying, Q., Zhang, Z., 2025. The North American greenhouse gas budget: emissions, removals, and integration for CO_2, CH_4, and N_2O (2010–2019): results from the Second Regional Carbon Cycle Assessment and Processes Study (RECCAP2). Glob. Biogeochem. Cycles 39, e2024GB008310.
Rodríguez-Fernández, N.J., Mialon, A., Mermoz, S., Bouvet, A., Richaume, P., Al Bitar, A., Al-Yaari, A., Brandt, M., Kaminski, T., Le Toan, T., Kerr, Y.H., Wigneron, J. P., 2018. An evaluation of SMOS L-band vegetation optical depth (L-VOD) data sets: high sensitivity of L-VOD to above-ground biomass in Africa. Biogeosciences 15 (14), 4627–4645.
Saleh, K., Wigneron, J.P., de Rosnay, P., Calvet, J.C., Kerr, Y.H., 2006. Semi-empirical regressions at l-band applied to surface soil moisture retrievals over grass. Remote Sens. Environ. 101 (3), 415–426.
Saleh, K., Wigneron, J.P., Waldteufel, P., de Rosnay, P., Schwank, M., Calvet, J.C., Kerr, Y.H., 2007. Estimates of surface soil moisture under grass covers using L-band radiometry. Remote Sens. Environ. 109 (1), 42–53.
Schlenz, F., Fallmann, J., Marzahn, P., Loew, A., Mauser, W., 2012. Characterization of rape field microwave emission and implications to surface soil moisture retrievals. Remote Sens. 4 (1), 247–270.
Scholze, M., Kaminski, T., Knorr, W., Voßbeck, M., Wu, M., Ferrazzoli, P., Kerr, Y., Mialon, A., Richaume, P., Rodríguez-Fernández, N., Vittucci, C., Wigneron, J.P., Mecklenburg, S., Drusch, M., 2019. Mean European carbon sink over 2010–2015 estimated by simultaneous assimilation of atmospheric CO_2, soil moisture, and vegetation optical depth. Geophys. Res. Lett. 46 (23), 13796–13803.
Schwank, M., Wigneron, J.P., Lopez-Baeza, E., Volksch, I., Matzler, C., Kerr, Y.H., 2012. Lband radiative properties of vine vegetation at the MELBEX III SMOS Cal/Val site. IEEE Trans. Geosci. Remote Sens. 50, 1587–1601.
Shen, A., Ma, Y., Li, Y., Hong, P., Niu, Z., Zhang, Y., Xiao, J., Zhang, D., 2025. RFAGB Model: a new machine learning model for microplastic inversion based on remotely sensed data in Bohai Sea. Water Res. 287, 124490.
Sorensen, D.C., 1982. Newton's method with a model trust region modification. SIAM J. Numer. Anal. 19 (2), 409–426.
Tikhonov, A.N., 1963. Solution of incorrectly formulated problems and the regularization method. Dokl. Akad. Nauk 151, 1035–1038.
Ulaby, F.T., Jedlicka, R.P., 1984. Microwave dielectric properties of plant materials. IEEE Trans. Geosci. Remote Sens. 22 (4), 406.
Van de Griend, A.A., Wigneron, J.P., 2004a. The b-factor as a function of frequency and canopy type at H-polarization. IEEE Trans. Geosci. Remote Sens. 42 (4), 786–794.
Van de Griend, A.A., Wigneron, J.P., 2004b. On the measurement of microwave vegetation properties: some guidelines for a protocol. IEEE Trans. Geosci. Remote Sens. 42 (10), 2277–2289.
Vittucci, C., Ferrazzoli, P., Richaume, P., Kerr, Y., 2017. Effective scattering albedo of forests retrieved by SMOS and a three-parameter algorithm. IEEE Trans. Geosci. Remote Sens. Lett. 14 (12), 2260–2264.
Vittucci, C., Ferrazzoli, P., Kerr, Y.H., Richaume, P., Laurin, G.V., Guerriero, L., 2018. Analysis of vegetation optical depth and soil moisture retrieved by SMOS over tropical forests. IEEE Trans. Geosci. Remote Sens. Lett. 16 (4), 504–508.
Vittucci, C., Laurin, G.V., Tramontana, G., Ferrazzoli, P., Guerriero, L., Papale, D., 2019. Vegetation optical depth at L-band and above ground biomass in the tropical range: evaluating their relationships at continental and regional scales. Int. J. Appl. Earth Obs. Geoinf. 77, 151–161.
Vittucci, C., Guerriero, L., Ferrazzoli, P., Richaume, P., Kerr, Y.H., 2021. SMOS L-VOD retrieved by level 2 algorithm and its correlation with GEDI LIDAR products. IEEE J. Sel. Top. Appl. Earth Obs. Remote Sens. 14, 11870–11878.
Vittucci, C., Guerriero, L., Ferrazzoli, P., 2023. Influence of vegetation height, plant area index and forest intactness on SMOS L-VOD, for different seasons and latitude ranges. IEEE Trans. Geosci. Remote Sens. 61, 5301911.
Walker, V.A., Hornbuckle, B.K., Cosh, M.H., Prueger, J.H., 2019. Seasonal evaluation of SMAP soil moisture in the U.S. Corn Belt. Remote Sens. 11, 2488.
Walker, V.A., Wallace, V., Yildirim, E., Eichinger, W.E., Cosh, M.H., Hornbuckle, B.K., 2023. From field observations to temporally dynamic soil surface roughness retrievals in the U.S. Corn Belt. Remote Sens. Environ. 287, 113458.
Wang, J.R., Choudhury, B.J., 1981. Remote sensing of soil moisture content over bare field at 1.4 GHz frequency. J. Geophys. Res. Oceans 86 (C6), 5277–5282.
Wang, H.Q., Magagi, R., Goïta, K., 2018. Potential of a two-component polarimetric decomposition at C-band for soil moisture retrieval over agricultural fields. Remote Sens. Environ. 217, 38–51.
Wang, M., Fan, L., Frappart, F., Ciais, P., Sun, R., Liu, Y., Li, X., Liu, X., Moisy, C., Wigneron, J.P., 2021a. An alternative AMSR2 vegetation optical depth for monitoring vegetation at large scales. Remote Sens. Environ. 263, 112556.
Wang, H.Q., Magagi, R., Goïta, K., Colliander, A., Jackson, T., McNairn, H., Powers, J., 2021b. Soil moisture retrieval over a site of intensive agricultural production using airborne radiometer data. Int. J. Appl. Earth Obs. Geoinf. 97, 102287.
Wigneron, J.P., Laguerre, L., Kerr, Y.H., 2001. A simple parameterization of the L-band microwave emission from rough agricultural soils. IEEE Trans. Geosci. Remote Sens. 39 (8), 1697–1707.
Wigneron, J.P., Pardé, M., Waldteufel, P., Chanzy, A., Kerr, Y., Schmidl, S., Skou, N., 2004. Characterizing the dependence of vegetation model parameters on crop structure, incidence angle, and polarization at L-band. IEEE Trans. Geosci. Remote Sens. 42 (2), 416–425.
Wigneron, J.P., Kerr, Y., Waldteufel, P., Saleh, K., Escorihuela, M.J., Richaume, P., Ferrazzoli, P., de Rosnay, P., Gurney, R., Calvet, J.C., Grant, J.P., Guglielmetti, M., Hornbuckle, B., Mätzler, C., Pellarin, T., Schwank, M., 2007. L-band microwave emission of the biosphere (L-MEB) model: description and calibration against experimental data sets over crop fields. Remote Sens. Environ. 107, 639–655.
Wigneron, J.P., Chanzy, A., Kerr, Y.H., Lawrence, H., Shi, J.C., Escorihuela, M.J., Mironov, V., Mialon, A., Demontoux, F., de Rosnay, P., Saleh-Contell, K., 2011.

Evaluating an improved parameterization of the soil emission in L-MEB. IEEE Trans. Geosci. Remote Sens. 49 (4), 1177–1189.
Wigneron, J.P., Jackson, T.J., O'Neill, P., De Lannoy, G., de Rosnay, P., Walker, J.P., Ferrazzoli, P., Mironov, V., Bircher, S., Grant, J.P., Kurum, M., 2017. Modelling the passive microwave signature from land surfaces: a review of recent results and application to the L-band SMOS & SMAP soil moisture retrieval algorithms. Remote Sens. Environ. 192, 238–262.
Wigneron, J.P., Fan, L., Ciais, P., Bastos, A., Brandt, M., Chave, J., Saatchi, S., Baccini, A., Fensholt, R., 2020. Tropical forests did not recover from the strong 2015–2016 El Niño event. Sci. Adv. 6 (6), eaay4603.
Wilson, W.J., Yueh, S.H., Dinardo, S.J., Chazanoff, S.L., Kitiyakara, A., Li, F.K., Rahmat-Samii, Y., 2001. Passive active L- and S-band (PALS) microwave sensor for ocean salinity and soil moisture measurements. IEEE Trans. Geosci. Remote Sens. 39 (5), 1039–1048.
Xiao, Z., Liang, S., Wang, J., Xiang, Y., Zhao, X., Song, J., 2016. Long-time-series global land surface satellite leaf area index product derived from MODIS and AVHRR surface reflectance. IEEE Trans. Geosci. Remote Sens. 54 (9), 5301–5318.
Xu, Z.Z., Chen, J., Wang, Y., Li, H.Q., Chen, F.J., Fan, Y.E., 2019. Sensitivity experiments of a stochastically perturbed parameterizations (SPP) scheme for mesoscale precipitation ensemble prediction. Acta. Meteor. Sin. 77 (05), 849–868.
Yan, S., Jiang, L., Chai, L., Yang, J., Kou, X., 2015. Calibration of the L-MEB Model for croplands in HiWATER using PLMR observation. Remote Sens. 7 (8), 10878–10897.
Ye, N., Zeng, Z., Zhou, J., Zhu, L., Duan, Y., Wu, Y., Wu, J., Zeng, H., Gu, Q., Wang, X., Zhou, C., 2024. Ood-control: generalizing control in unseen environments. IEEE Trans. Pattern Anal. Mach. Intell. 46 (11), 7421–7433.
Zeng, J., Chen, K.S., Bi, H., Chen, Q., 2016. A preliminary evaluation of the SMAP radiometer soil moisture product over United States and Europe using ground-based measurements. IEEE Trans. Geosci. Remote Sens. 54 (8), 4929–4940.
Zeng, Y.L., Hao, D.L., Huete, A., Dechant, B., Berry, J., Chen, J.M., Joiner, J., Frankenberg, C., Bond-Lamberty, B., Ryu, Y., Xiao, J.F., Asrar, G.R., Chen, M., 2022. Optical vegetation indices for monitoring terrestrial ecosystems globally. Nat. Rev. Earth Environ. 3, 477–493.
Zobeck, T.M., Onstad, C.A., 1987. Tillage and rainfall effects on random roughness: a review. Soil Tillage Res. 9, 1–20.
Zotta, R.M., van der Schalie, R., Preimesberger, W., Mösinger, L., De Jeu, R., Dorigo, W. A., 2023. Vegetation optical depth [in state of the climate in 2022]. B. Am. Meteorol. Soc. 104, S110–S112.
Zribi, M., Gorrab, A., Baghdadi, N., 2014. A new soil roughness parameter for the modelling of radar backscattering over bare soil. Remote Sens. Environ. 152, 62–73.